Variations of Raindrop Size Distribution and Radar Retrieval in Outer Rainbands of Typhoon Mangkhut (2018)

Jingjing LYU[1], Huiwen XIAO[1,4], Yuchun DU[1,4], Lina SHA[1], Yuqing DENG[1,4], Weikai JIA[1], Shengjie NIU[1], Yue ZHOU[2*], and Guqian PANG[3]

1 *Collaborative Innovation Center on Forecast and Evaluation of Meteorological Disasters (CIC-FEMD), Key Laboratory for Aerosol–Cloud–Precipitation of China Meteorological Administration, Nanjing University of Information Science &Technology, Nanjing* 210044
2 *Hubei Key Laboratory for Heavy Rain Monitoring and Warning Research, Institute of Heavy Rain, China Meteorological Administration, Wuhan* 430205
3 *Climate Center of Guangdong Province, Guangzhou* 510080
4 *College of Earth and Planetary Sciences, University of Chinese Academy of Sciences, Beijing* 100049

(Received July 20, 2021; in final form April 11, 2022)

ABSTRACT

The evolution of the microphysical properties of raindrops from Typhoon Mangkhut's outer rainbands as the storm made landfall in South China in September 2018 was investigated. The observations by three two-dimensional video disdrometers deployed in central Guangdong Province were analyzed concurrently. It was found that the radial distribution of the median volume diameter (D_0) and normalized intercept parameter (N_w) varied in different stages, and that raindrops smaller than 3.0 mm contributed more than 99% of the total precipitation. Considering the characteristics of precipitation in the typhoon outer rainband, a modified stratiform rain (SR)–convective rain (CR) separator line is proposed based on D_0 and N_w scatterplots. Meanwhile, an "S–C likelihood index" is introduced, which was used to classify three rain types (SR, CR, and mixed rain). The CR results were highly consistent with those of the improved typhoon precipitation classification method based on rain rate. By calculating effectively the radar reflectivity factor (Z_e) in the Ku and Ka bands, D_0–Z_e and N_w–D_0 empirical relations were thereby derived for improving the accuracy of rainfall retrieval. Among the four quantitative precipitation estimators using S-band dual-polarimetric radar parameters simulated by the T-matrix method, the estimator that adopted the specific differential phase and differential reflectivity was found to be the most effective for both SR and CR.

Key words: typhoon, two-dimensional video disdrometer, drop size distribution, axis ratio, quantitative precipitation estimation

Citation: Lyu, J. J., H. W. Xiao, Y. C. Du, et al., 2022: Variations of raindrop size distribution and radar retrieval in outer rainbands of Typhoon Mangkhut (2018). *J. Meteor. Res.*, **36**(3), 500–519, doi: 10.1007/s13351-022-1134-2.

1. Introduction

Strong winds and heavy precipitation associated with typhoons can cause severe economic losses and human casualties in the affected areas. Severe typhoons frequently occur in China, amounting to CNY 25 billion in annual economic losses (Liu et al., 2009). Improving the quantitative precipitation estimation (QPE) of typhoons is of great significance for mitigating these impacts, particularly for the hardest-hit coastal areas. Therefore, understanding the microphysical processes occurring in the heavy rainfall of typhoons is crucial (Wang et al., 2016; Wen et al., 2018; Zhao et al., 2019).

Analysis of the microphysical characteristics of precipitation is based on the drop size distribution (DSD). DSD varies significantly in different climate regions and

Supported by the National Key Research and Development Program of China (2018YFC1507905), National Natural Science Foundation of China (41675136 and 41875170), National Undergraduate Innovation and Entrepreneurship Training Program (201910300040Z), Opening Project of Key Laboratory for Aerosol–Cloud–Precipitation of China Meteorological Administration (KDW1405), Natural Science Foundation of Guangdong Province of China—Major Basic Research and Cultivation Projects (2015A030308014), and Guangxi Key Research and Development Program (AB20159013).

*Corresponding author: zhouyue8510@163.com

weather systems owing to the contrast in microphysical processes (Maki et al., 2001; Bringi et al., 2003; Chakravarty and Raj, 2013). Based on such differences in DSD, precipitation systems can usually be divided into convective rain (CR) and stratiform rain (SR) (Tokay and Short, 1996; Testud et al., 2001; Bringi et al., 2003; Chen et al., 2017). The former can be further subdivided into maritime and continental CR (Bringi et al., 2003), which themselves show differences in DSD. For example, the number concentration of continental CR with diameter > 4 mm is larger than that in maritime CR. Chang et al. (2009) used a two-dimensional video disdrometer (2DVD) in northern Taiwan to study the DSD of 13 typhoons that landed in Taiwan and found that the DSD of typhoon precipitation over the ocean was closer to maritime CR, whereas over land, it tended to be between the DSD of maritime and continental CR. Therefore, DSD has a guiding significance for distinguishing precipitation types. It has been noted that DSDs across different precipitation systems are related to differences in microphysical processes (Maki et al., 2001; Bringi et al., 2003; Chakravarty and Raj, 2013), which can further enable us to employ the DSD to establish relationships between precipitation types and corresponding microphysical processes. In addition, the typhoon has long been recognized as an eyewall/rainband complex (Willoughby et al., 1984; Houze, 2010); and generally, two types of typhoon rainbands can be defined based on their positions and movement relative to the typhoon center—namely, inner and outer rainbands (Wu et al., 2018). Most studies have focused on using polarimetric radar observations and retrieved DSDs to analyze the kinematics and microphysical processes as well as the vertical structure in the inner and/or outer rainbands of typhoons in the eastern (Wang et al., 2016; Wang et al., 2018; Wu et al., 2018) and southern (Zheng et al., 2021) coastal areas of China. Recently, Bao et al. (2019, 2020a) showed that, even for the same typhoon, the DSD characteristics of different rainbands might have obvious discrepancies. The mean raindrop diameter D_m (concentration $\lg N_w$) was found to generally decrease (increase) radially from the typhoon center (Bao et al., 2020b). Thus, further analysis of the microphysical characteristics of raindrops using disdrometer data is critical not only to thoroughly investigate the relationship between DSD and different microphysical processes of the precipitation of typhoon rainbands, but also to improve the QPE algorithm of weather radar with different wavelengths (especially dual-polarization radar). Early studies on QPE used Doppler radar to establish relationships between the reflectivity Z and rainfall rate R (e.g., Ulbrich and Lee, 2002; Tokay et al., 2008; Chen et al., 2012). Ulbrich and Lee (2002) fitted three Z–R relationships for Tropical Storm Helene and proposed that applying advanced radar technology to DSD retrieval will improve the accuracy of the Z–R relationship. In recent studies, dual-polarimetric radars have been favored over conventional Doppler radars because the former provide additional parameters for reflecting the microphysical characteristics of the precipitation system. Therefore, dual-polarimetric radar can effectively improve the accuracy of QPE (Zhao et al., 2019) and facilitate the establishment of QPE models of radar parameters that are suitable for specific areas (Cao et al., 2008; Chang et al., 2009; Wang et al., 2016; Wen et al., 2018). Therefore, introducing dual-polarimetric radar parameters can significantly reduce the uncertainty in precipitation estimation caused by changes in the DSD. However, Lee (2006) reported that when the fitted relationship includes the specific differential phase K_{DP} and the actual R is less than 7 mm h^{-1}, the error of the estimated R will be greater than that determined by the traditional Z–R relationship. Consequently, the topic is worthy of further study.

Typhoon rainband precipitation exhibits obvious spatial and temporal inhomogeneities (Yue et al., 2006; Huang et al., 2012). The large uncertainties in single-point observations lead to the ineffective reflection of differences in the rainband precipitation processes. More accurate QPE requires a deep understanding of the precipitation's microphysical characteristics (Ji et al., 2019); therefore, analysis of the DSD and drop shape relation (DSR) of the precipitation is crucial. Most previous observational studies (e.g., Chen et al., 2012; Tang et al., 2014; Wang et al., 2016; Bao et al., 2019; Wu et al., 2019) have been based on data from one-dimensional disdrometers. Under strong winds, however, accurate particle size, falling velocity, and DSR data cannot be obtained. In contrast, 2DVDs can directly obtain the size, quantity, falling velocity, shape, and horizontal deviation direction of the raindrops (Kruger and Krajewski, 2002). The 2DVDs not only improve the accuracy of the QPE algorithm using ground-based dual-polarization radar, but also provide verification data for improving the retrieval algorithm for Global Precipitation Measurement (GPM) Dual-Frequency Precipitation Radar (DPR) raindrop spectra. However, only a few previous studies have used 2DVDs to observe the microphysical characteristics of typhoon precipitation (e.g., Wang et al., 2016; Wen et al., 2018); and of these, most were limited to the precipitation characteristics recorded near a single station. Using a single disdrometer to study the spatial characteristics in typhoon outer rainbands is unrealistic.

Therefore, further research is needed in which multiple disdrometers are applied to elucidate the microphysical characteristics of precipitation particles in typhoon rainbands, which is the motivation behind the present study.

The rest of this paper is organized as follows. The data sources and processing are described in Section 2, and Section 3 outlines the synoptic background and vertical structure of Typhoon Mangkhut prior to landfall. The spatiotemporal evolution of the microphysical characteristics of the outer rainbands after landfall is discussed. Then, the DSR and classification of the precipitation types are evaluated to establish a QPE model suitable for the southern coast of China. Moreover, this work investigates the application of DSD for the improvement of GPM/DPR. The paper concludes with a summary in Section 4.

2. Data sources and processing

2.1 *Experimental setup*

The 2DVD observation data of Fogang (FG), Longmen (LM), and Xinfeng (XF) stations in Guangdong Province, China, were used to investigate the microphysical characteristics of the outer rainbands of Typhoon Mangkhut. Table 1 shows the locations of the three stations. The 2-min-average wind speed data recorded by the automated weather stations at these three sites were also used in the analysis. These three stations are located within the range of precipitation after the typhoon made landfall (Fig. 1). The track, center pressure, and maximum wind speed of Typhoon Mangkhut were obtained from the China Meteorological Administration (https://tcdata.typhoon.org.cn/zjljsjj_sm.html; Ying et al., 2014; Lu et al., 2021). To fully understand the synoptic background near the rainband before and after the typhoon made landfall, this study used the interpolated ERA5 data (fifth major global reanalysis produced by ECMWF; https://www.ecmwf.int/), with a horizontal resolution of 0.25° × 0.25° and 27 barometric pressure levels, which are provided four times daily at 0000, 0600, 1200, and 1800 UTC 16 September 2018. The dataset contains meteorological variables such as temperature, relative humidity, water vapor mixing ratio, meridional and zonal wind speed, and geopotential height.

In addition, the sounding data recorded at Qingyuan (QY) at 0600 and 1200 UTC 16 September were used. These data provide information on air pressure, temperature, relative humidity, geopotential height, wind direction, and wind speed from the ground to 100 hPa with a time interval of 1 s. Sounding station QY is located between the typhoon track and the rainbands (Fig. 1). Outer rainbands usually develop farther outside the eyewall, more than 150–200 km from the typhoon center (Willoughby et al., 1984; Wang, 2002; Skwira et al., 2005; Wang et al., 2018). During the movement of the typhoon, the shortest distances between the typhoon center and the stations are all larger than 200 km (243.7, 264.7, and 292.3 km for FG, LM, and XF, respectively). It is reasonable to consider that FG, LM, and XF are located in the outer rainbands, while QY may have been affected by the inner rainband as its closest approach is only 203.7 km. When the typhoon made landfall, stations QY, FG, LM, and XF are all within the seven Beaufort scale wind circle; therefore, the results effectively reflect the synoptic background near the rainbands caused by the typhoon. By using the QY data, we calculated the lifting condensation level, *K*-index, convective available potential energy (CAPE), and other relevant parameters that reflect the state of the atmosphere to assist in the analysis of the synoptic background condi-

Table 1. Location and altitude of Fogang (FG), Longmen (LM), and Xinfeng (XF) stations

	Fogang	Longmen	Xinfeng
Location	23.88°N, 113.52°E	23.78°N, 114.24°E	24.05°N, 114.19°E
Altitude (m)	97.2	85.5	199.3

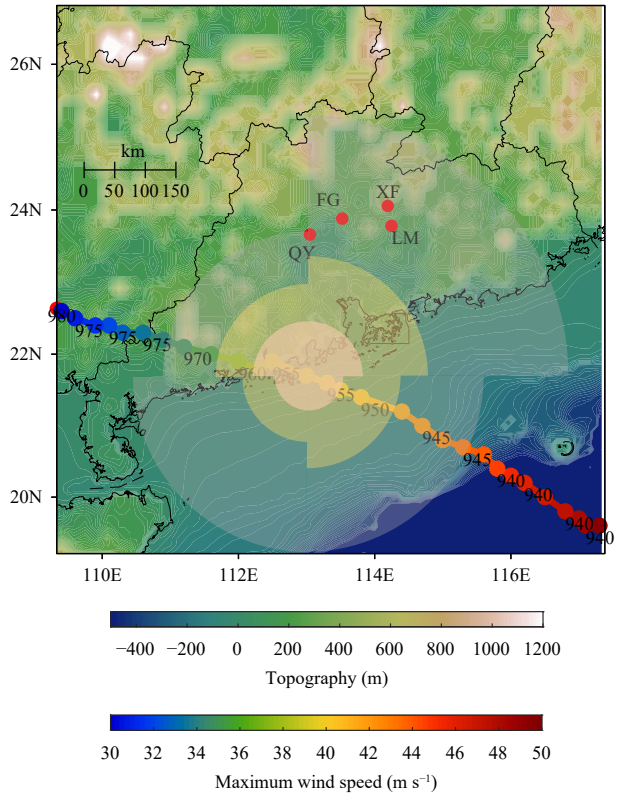

Fig. 1. Topographic information for the area near the rainbands in addition to data on the typhoon's landfall pathway and intensity. The pink, yellow, and gray sectors represent the 12, 10, and 7 Beaufort scale wind circles, respectively.

tions of the rainbands during the landfall of Typhoon Mangkhut.

The 2DVD instrument employed in this study can quickly scan precipitation from two mutually perpendicular directions. The area of overlapping observation is approximately 10 × 10 cm^2, and the light sheets are spaced (nominally) 6.2 mm apart. The imaging grid resolution for raindrops is finer than 0.2 mm, in the horizontal and vertical directions. The 2DVD provides a wide range of precipitation information, such as the precipitation amount, DSD, raindrop falling speed, and axis ratio of the precipitation particles. Details on DSD are provided elsewhere (Kruger and Krajewski, 2002). Many previous studies have reported that turbulence and splash caused by wind can lead to oversampling of small raindrops (< 1 mm in diameter) in the 2DVD data. In this work, a filter method proposed by Kruger and Krajewski (2002) is applied to preprocess the 2DVD data:

$$\left|V_{\rm obs} - V_{\rm exp}\right| < cV_{\rm exp}, \tag{1}$$

where $V_{\rm obs}$ is the observed raindrop falling velocity, $V_{\rm exp}$ reflects the relationship between the raindrop diameter and the falling velocity (Brandes et al., 2002), and the coefficient c is 0.4 (Kruger and Krajewski, 2002). All data must be filtered through the above method to remove the oversampling error before making subsequent calculations. As shown in Fig. 2, the average falling velocity of raindrops observed by the 2DVD instrument was in good agreement with the terminal drop velocity of raindrops derived from laboratory measurements proposed by Brandes et al. (2002). This demonstrates that the observations made by 2DVD are reliable. The data were distributed mainly from 0200 to 1800 UTC 16 September 2018. After quality-control was performed on the data, a total of 2,931,754 drop counts were obtained from the 2DVD at 15-s intervals. Lastly, the observations were processed into a 1-min temporal resolution.

2.2 *Integral rainfall parameters*

The gamma function can effectively represent the DSD (Ulbrich, 1983) as

$$N(D) = N_0 D^{\mu} \exp(-\Lambda D), \tag{2}$$

where N_0 (mm^{-1} m^{-3}) is the intercept related to the number concentration of the raindrops, μ (dimensionless) is the shape parameter, and Λ (mm^{-1}) is the slope parameter. These three parameters are usually calculated by the second, fourth, and sixth moments, respectively, in the truncated moment method (Ulbrich and Atlas, 1998). When $\mu > 0$ (< 0), the distribution curve bends upward (downward); a smaller (larger) Λ value relates to a larger (smaller) number concentration of large raindrops. The

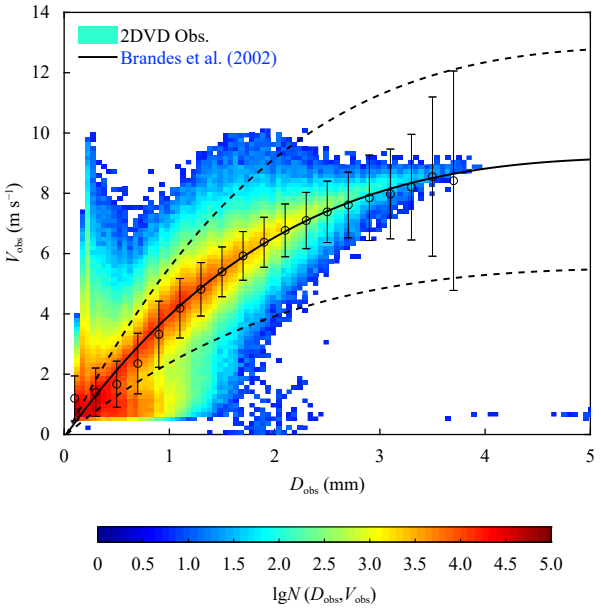

Fig. 2. Velocity–diameter combination and drop counts on a logarithm scale (color shading) obtained by 2DVD observations. The measured fall velocity of the raindrops and the mean and standard deviation of the measured fall velocity as a function of diameter are given. The black line represents the terminal drop velocity proposed by Brandes et al. (2002), and the two dashed lines represent the ±40% filter of the drops.

microphysical parameters of rainfall play a role in shaping our understanding of the precipitation processes of rainbands. These parameters include the total concentration of raindrops $N_{\rm t}$ (m^{-3}), liquid water content (LWC; g m^{-3}), R (mm h^{-1}), mass-weighted mean diameter $D_{\rm m}$ (mm), generalized intercept parameter $N_{\rm w}$ (mm^{-1} m^{-3}), and median volume diameter D_0 (mm). When the DSD is determined, $N_{\rm t}$, LWC, and R can be expressed as (Cao et al., 2012)

$$N_{\rm t} = \sum_{i=1}^{L} N(D_i)\Delta D_i, \tag{3}$$

$$\mathrm{LWC} = \frac{\pi}{6000}\sum_{i=1}^{L} D_i^3 N(D_i)\Delta D_i, \tag{4}$$

$$R = \frac{6\pi}{10^4}\sum_{i=1}^{L} D_i^3 V_i N(D_i)\Delta D_i, \tag{5}$$

where D_i is the equivalent volume diameter of the particle. In this case, the raindrops are classified into several bins according to the equivalent volume diameter of the raindrop. In addition, i is the serial number of the bins, L is the total number of bins, ΔD_i is the corresponding diameter interval, V_i is the falling velocity of the particle, and $N(D_i)$ is the number concentration of raindrops with diameters ranging from $D_i - 0.5\Delta D_i$ to $D_i +$

$0.5\Delta D_i$. The DSD can vary significantly among regions and times, making it challenging to compare raindrops in different precipitation processes.

The normalized gamma function (Testud et al., 2001), which is also widely used to describe the DSD, enables comparison of the DSD in different regions (Zhang et al., 2017). Moreover, this function helps improve the GPM (Chen et al., 2017) and assimilate the remote sensing estimation of precipitation into satellite systems. The normalized gamma function can be expressed as (Gorgucci et al., 2001, 2002; Chandrasekar et al., 2005)

$$N(D) = N_{\rm w} f(\mu) \left(\frac{D}{D_0}\right)^{\mu} {\rm e}^{-(3.67+\mu)\left(\frac{D}{D_0}\right)}, \tag{6}$$

and

$$f(\mu) = \frac{6}{3.67^4} \frac{(3.67+\mu)^{(\mu+4)}}{\Gamma(\mu+4)}, \tag{7}$$

where $N_{\rm w}$ and D_0 are obtained by the following expressions (Bringi et al., 2003; Chandrasekar et al., 2005):

$$\frac{1}{2}{\rm LWC} = \frac{\pi}{6}\rho_{\rm w} \cdot \int_0^{D_0} D^3 N(D)\,{\rm d}D, \tag{8}$$

$$N_{\rm w} = \frac{3.67^4}{\pi\rho_{\rm w}}\left(\frac{LWC}{D_0^4}\right), \tag{9}$$

where $\rho_{\rm w}$ (1000 kg m^{-3}) is the density of water, and the volume-weighted $D_{\rm m}$ (Chandrasekar et al., 2005) is defined as

$$D_{\rm m} = \frac{\sum_{i=1}^{L} D_i^4 V_i N(D_i)\Delta D_i}{\sum_{i=1}^{L} D_i^3 V_i N(D_i)\Delta D_i}. \tag{10}$$

2.3 *Polarimetric radar parameters*

The dual-polarimetric radar parameters used in this study include radar reflectivity in the horizontal (vertical) polarization $Z_{\rm h}$ ($Z_{\rm v}$), differential reflectivity $Z_{\rm DR}$, and $K_{\rm DP}$ in the S band. Seliga and Bringi (1976) found that if $Z_{\rm v}$ and $Z_{\rm DR}$ are applied to DSD retrieval, a one-to-one correspondence exists between $Z_{\rm DR}$ and D_0, and R is a function of N_0 and D_0 (assuming that the terminal drop velocity is known).

$K_{\rm DP}$ mainly relies on the LWC and is immune to radar attenuation and calibration, and sometimes partial beam blockage. This value is widely used for quantitative radar precipitation estimation (Bringi and Chandrasekar, 2001). $Z_{\rm h}$, $Z_{\rm v}$, and $K_{\rm DP}$ can be calculated from the DSD (Zhang et al., 2001) using the T-matrix scattering technique (Ishimaru, 1991) as follows:

$$Z_{\rm h,v} = \frac{4\lambda^4}{\pi^4 |K_{\rm w}|^2} \int_{D_{\rm min}}^{D_{\rm max}} \left| f_{\rm hh,vv}(\pi, D) \right|^2 N(D)\,{\rm d}D, \tag{11}$$

$$Z_{\rm DR} = 10\lg\frac{Z_{\rm v}}{Z_{\rm h}}, \tag{12}$$

$$K_{\rm DP} = \frac{180\lambda}{\pi} \int_{D_{\rm min}}^{D_{\rm max}} {\rm Re}\left[f_{\rm hh}(0,D) - f_{\rm vv}(0,D)\right] N(D)\,{\rm d}D. \tag{13}$$

Here, λ represents the radar wavelength, $K_{\rm w}$ is the dielectric factor of water, $f_{\rm hh,vv}(\pi,D)$ represents the backscattering amplitude, and Re represents the real part of the complex number.

3. Results and discussion

3.1 *Description of synoptic background*

Typhoon Mangkhut moved northwest following the steering flow on the edge of a subtropical high (Fig. 3) and made landfall in Guangdong at about 0900 UTC 16 September. The wind velocity in the typhoon eyewall reached 45 m s^{-1} at the time of landing. The lowest pressure was 955 hPa. Figures 3a and 3b indicate that the typhoon kept moving northeastward at 0000 UTC and 0600 UTC 16 September. Its intensity increased prior to its landfall, with shrinkage of the eyewall (Figs. 3a, b). After the typhoon made landfall, the central pressure gradually increased and the outer closed wind field began to shatter and weaken, as shown in the wind field diagrams at 1200 and 1800 UTC 16 September (Figs. 3c, d). Typhoon Mangkhut also carried a large amount of water vapor. In particular, the mixing ratio in the center and peripheral areas of the typhoon at 850 hPa exceeded 16 g kg^{-1} (Fig. 3).

The sounding profile at Station QY at 0600 UTC 16 September (Fig. 4) shows a deep, wet layer from the lifting condensation level from 970 hPa (332 m) to about 400 hPa (7492 m). Water vapor was abundant, and the height of the melting layer was 5 km; warm clouds below this layer were dominant. A thermal inversion layer was present from 700 to 500 hPa with a K-index of 37, and the CAPE was 593.8 J kg^{-1}. These factors indicate the accumulation of unstable energy in the atmosphere. The vertical wind shear was weak from 750 hPa (3 km) to 550 hPa (6 km), which was conducive to the accumulation of latent heat through condensation and provided conditions for the occurrence of severe convective weather. Meanwhile, the CAPE reached 131.5 J kg^{-1} at 1200 UTC 16 September, which is significantly lower than that at 0600 UTC, indicating the severe convective weather released the unstable energy of the atmosphere during this period.

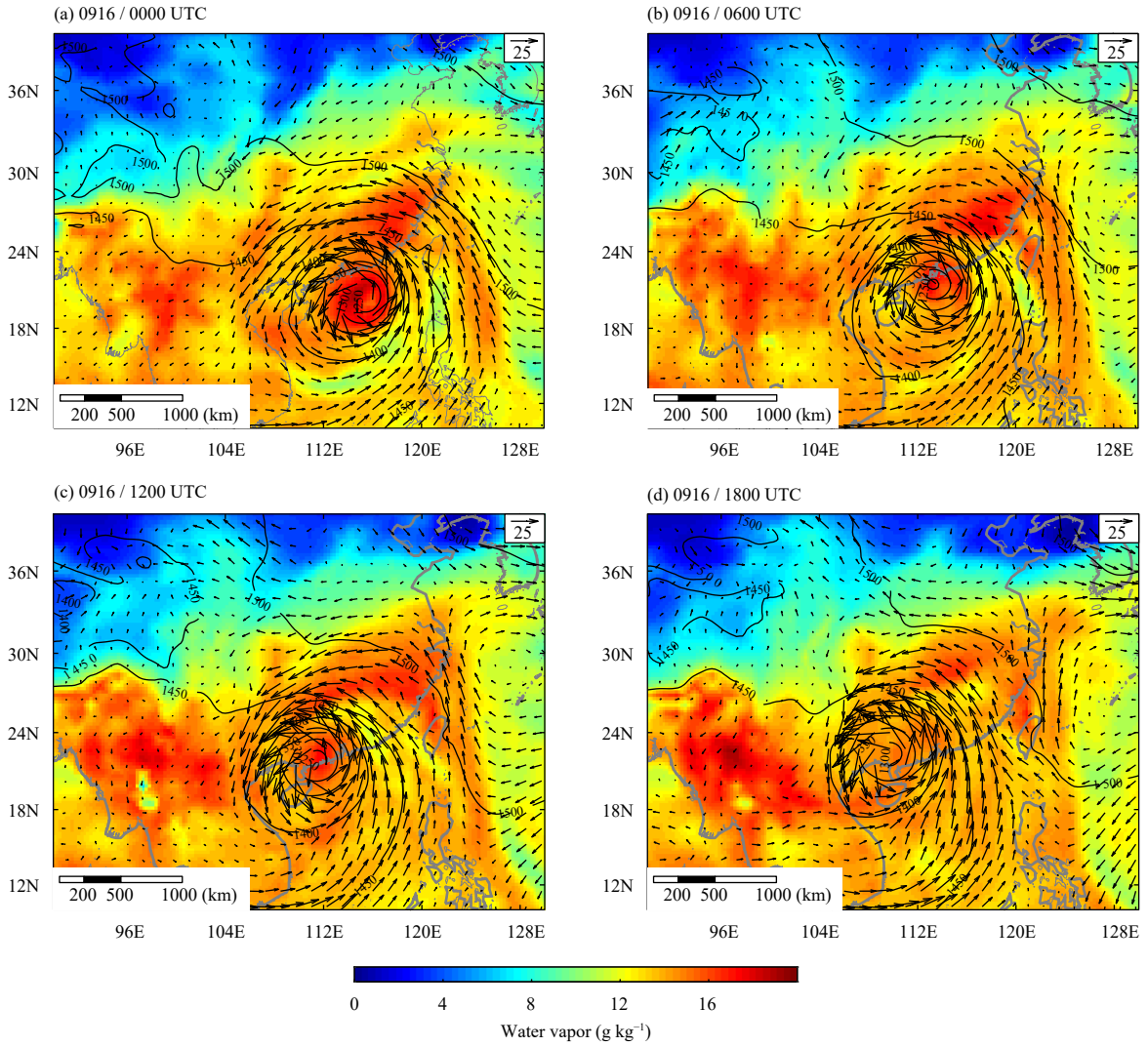

Fig. 3. Mixing ratio of water vapor (shading; g kg^{-1}), wind field (vector; m s^{-1}), and geopotential height (contour; gpm) at 850 hPa obtained from ERA5 at (a) 0000, (b) 0600, (c) 1200, and (d) 1800 UTC 16 September. The reference wind vectors (25 m s^{-1}) are also shown in the upper right, and the scale is shown in the lower left.

3.2 *Evolution of microphysical characteristics of raindrops*

3.2.1 *DSD*

Figure 5 shows evolution of the microphysical characteristics of raindrops at stations FG, LM, and XF before and after Typhoon Mangkhut made landfall. To facilitate this analysis, those raindrops with diameters < 1, 1–3, and > 3 mm, are defined herein as small drops (SDR), medium drops (MDR), and large drops (LDR), respectively. According to the typhoon's landfall time provided by the China Typhoon Network (https://www.typhoon.org.cn/), as well as the distance between observation sites and the typhoon center, the process was divided into three stages: pre-landfall (1600 UTC 15–0900 UTC 16 September), landfall (0900–1200 UTC 16 September), and post-landfall (1200–2000 UTC 16 September).

Combined with the distance between the typhoon center and the stations, as well as the evolutionary characteristics of R in Fig. 5, most precipitation periods occurred within the range of about 250–400 km from the typhoon center. The typhoon center was in a northwest direction and kept approaching the three stations. During the pre-landfall stage, station LM was the first affected by the rainband as the typhoon approached, with the longest rainfall duration and the highest total number concentration of SDR (N_{SDR}, 7999.18 m^{-3}), the maximum raindrop diameter (4.0 mm), and the largest R (22.10 mm h^{-1}). Perhaps due to the influence of convective-scale elements in the rainband, 34 samples of R values exceeded 10 mm h^{-1} from 1550 UTC, which made the cumulative precipitation (28.21 mm) and corresponding microphys-

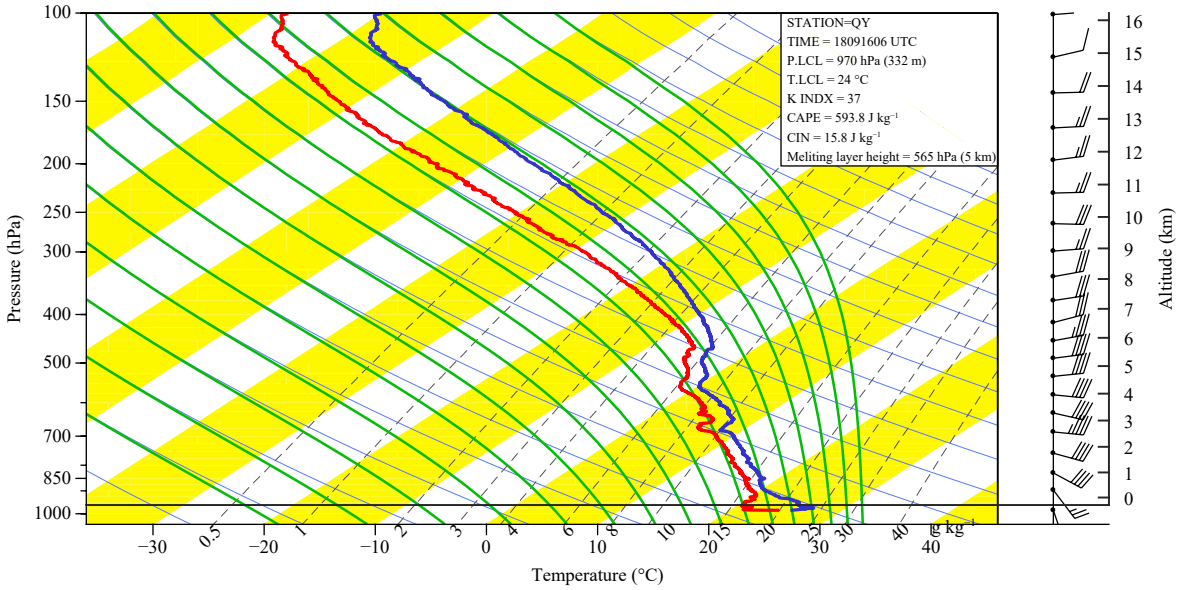

Fig. 4. Skew T–lg$p$ diagram and vertical wind profile at Station QY at 0600 UTC 16 September 2018. The blue and red lines represent the air temperature and dewpoint temperature profiles, respectively.

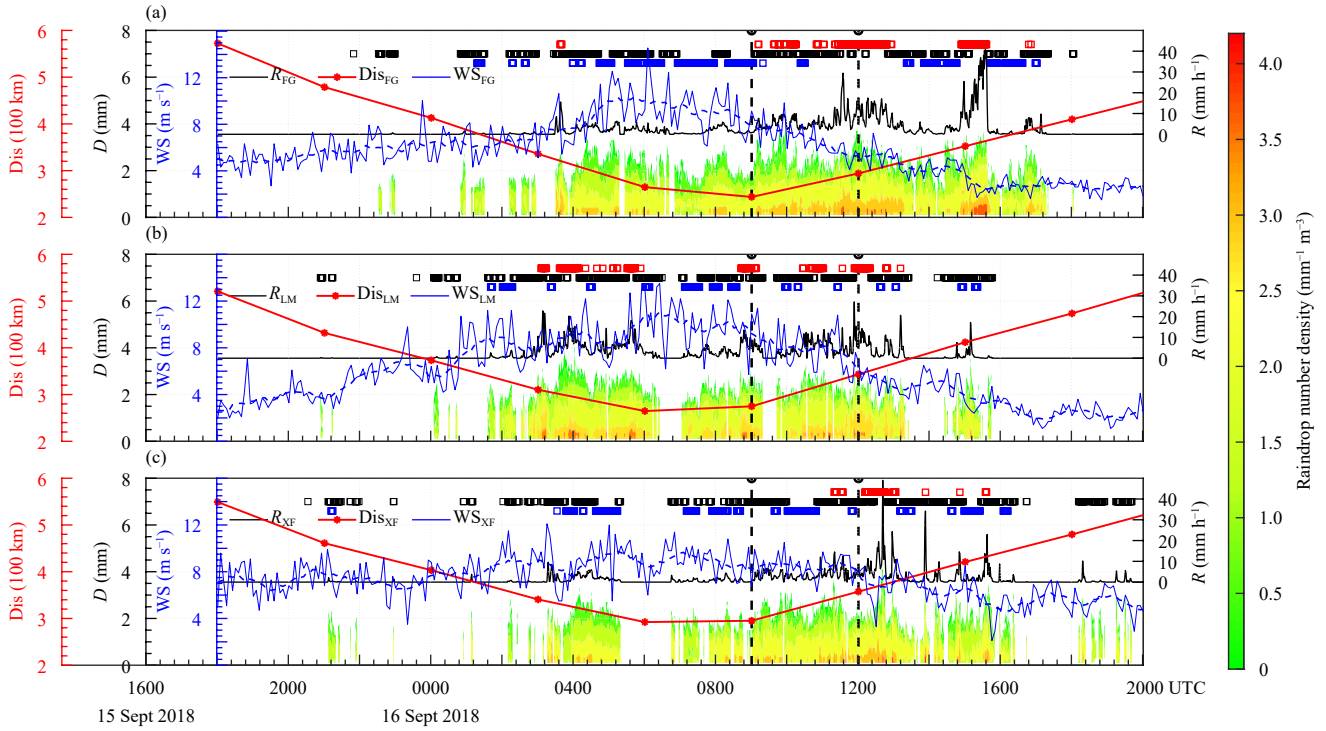

Fig. 5. Evolutions of DSDs observed at stations (a) FG, (b) LM, and (c) XF. The color shading represents the DSD in logarithmic units of mm^{-1} m^{-3}. The left- and right-hand black y-axes indicate the equivalent diameter D (mm) of raindrops and the calculated rain rate R (mm h^{-1}), respectively. The red and blue curves represent the distance between the observation sites and the typhoon center (Dis) and wind speed (WS; m s^{-1}), respectively. The two vertical black dashed lines separate the stages of pre-landfall, landfall, and post-landfall. For better understanding, SR, CR, and mixed rain samples are drawn as blue, red, and black squares, respectively, which are derived from a modified classification scheme based on Bao et al. (2019), as detailed in Section 3.3.

ical parameters much higher than those of the other two stations (FG and XF). Station FG was the closest station to the eyewall during landfall, with the maximum R of 29.40 mm h^{-1} at 1130 UTC, and N_{SDR} increased to 7026.02 m^{-3}. At station XF, the precipitation also increased during this period, and the concentration of rain-

drops with diameters < 0.5 mm increased significantly; however, the maximum R was not high, at 14.50 mm h^{-1}. During post-landfall, R at station FG increased rapidly to 40.80 mm h^{-1} at about 1550 UTC, and then weakened rapidly. During this period, N_{SDR} at FG increased rapidly and reached a maximum of 11989.41 m^{-3}. At the same time, the precipitation at stations XF and LM was in the dissipation stage. The precipitation at station LM at 1200 UTC was relatively weak; the maximum R was only 20.60 mm h^{-1}, and N_{SDR} changed slightly to 7041.90 m^{-3}. At station XF, a precipitation peak appeared at about 1300 UTC, and R reached 48.90 mm h^{-1}. Intermittent precipitation also appeared from 1400 to 1530 UTC, during which time N_{SDR} increased to a maximum value of 14882.82 m^{-3}.

The relevant microphysical parameters calculated from the DSD were divided into three stages, as shown in Table 2. These statistics correspond to the three stages of the evolution of Typhoon Mangkhut mentioned above, all of which are expressed as mean ± standard deviation. Table 2 further reflects the typhoon's evolution from a numerical perspective. Before Mangkhut made landfall, the precipitation at LM was relatively active, showing a larger average R (4.04 mm h^{-1}) than that at the other two stations.

During the landfall stage, the average R at the three stations increased significantly, particularly at FG and XF. The maximum average R appeared at FG (6.04 mm h^{-1}). During the post-landfall stage, R decreased somewhat, although the decrease was discernible solely at station LM; the average values of related microphysical parameters were still higher than those in the landfall stage. The average R at FG changed significantly during the three stages. The low value of 1.81 mm h^{-1} before the typhoon landed rapidly increased to 6.04 mm h^{-1} during landfall. After the typhoon had made landfall, the value remained high at 5.80 mm h^{-1}. In addition, the LWC increased from 0.10 to 0.35 g m^{-3} during the first two stages and decreased to 0.33 g m^{-3} after the typhoon landed. The variables D_0 and D_m increased to 1.31 mm during the landfall stage but showed values of about 1.22 mm during the other two stages. The variable $\lg N_w$ was also high during the landfall stage, at 3.94 mm^{-1} m^{-3}, and the average value decreased before and after landfall. Their values at LM and XF showed similar change characteristics. The differences in the evolution of the DSD characteristics over time at different sites show that the microphysical characteristics in the typhoon rainbands include obvious spatiotemporal inhomogeneities. It is worth mentioning that although SDR contributed more than 82.4% to N_t, most of its contribution to the total precipitation came from MDR (72.3%), indicating that the precipitation of Typhoon Mangkhut was mainly dominated by raindrops less than 3 mm in diameter.

Moreover, we further analyzed the radial distributions

Table 2. Mean ± standard deviation of relevant microphysical parameters and the contribution of raindrops in different diameter ranges (SDR/MDR/LDR) to N_t and R categorized by the stages of Typhoon Mangkhut's evolution

Location	Parameter	Pre-landfall	Landfall	Post-landfall
FG	LWC (g m^{-3})	0.10 ± 0.11	0.35 ± 0.23	0.33 ± 0.43
	R (mm h^{-1})	1.81 ± 1.94	6.04 ± 4.30	5.80 ± 8.00
	D_0 (mm)	1.22 ± 0.41	1.31 ± 0.19	1.21 ± 0.32
	D_m (mm)	1.23 ± 0.36	1.34 ± 0.19	1.23 ± 0.30
	$\lg N_w$ (mm^{-1} m^{-3})	3.45 ± 0.35	3.94 ± 0.20	3.79 ± 0.37
	Dis [mean (max, min)] (km)	337.8 [412.9, 264.7]	268.2 [294.1, 243.7]	381.1 [409.9, 352.3]
	Contribution to R (%)	31.03/68.08/0.89	17.77/80.45/1.78	32.10/67.06/0.84
	Contribution to N_t (%)	87.75/12.24/0.01	84.79/15.19/0.02	89.45/10.54/0.01
LM	LWC (g m^{-3})	0.23 ± 0.21	0.32 ± 0.21	0.21 ± 0.25
	R (mm h^{-1})	4.04 ± 3.94	5.36 ± 3.83	3.41 ± 4.32
	D_0 (mm)	1.32 ± 0.25	1.33 ± 0.17	1.14 ± 0.28
	D_m (mm)	1.31 ± 0.23	1.32 ± 0.15	1.16 ± 0.27
	$\lg N_w$ (mm^{-1} m^{-3})	3.60 ± 0.39	3.83 ± 0.24	3.69 ± 0.50
	Dis [mean (max, min)] (km)	316.1 [373.2, 264.7]	309.1 [343.4, 274.7]	442.7 [473.6, 411.9]
	Contribution to R (%)	20.82/78.63/0.55	16.43/83.33/0.25	35.10/64.20/0.74
	Contribution to N_t (%)	85.02/14.97/0	82.42/17.58/0	84.63/15.36/0.01
XF	LWC (g m^{-3})	0.09 ± 0.09	0.21 ± 0.13	0.20 ± 0.28
	R (mm h^{-1})	1.46 ± 1.50	3.49 ± 2.39	3.45 ± 5.57
	D_0 (mm)	1.19 ± 0.26	1.29 ± 0.22	1.17 ± 0.34
	D_m (mm)	1.20 ± 0.25	1.30 ± 0.21	1.18 ± 0.32
	$\lg N_w$ (mm^{-1} m^{-3})	3.40 ± 0.45	3.73 ± 0.27	3.68 ± 0.47
	Dis [mean (max, min)] (km)	345.4 [403.3, 292.3]	326.3 [357.4, 295.1]	450.3 [479.8, 420.8]
	Contribution to R (%)	29.24/70.20/0.55	20.10/78.44/0.57	35.51/63.51/0.98
	Contribution to N_t (%)	84.89/15.10/0.01	85.89/14.10/0.01	88.66/11.33/0.01

of the average D_0 and lgN_w from the typhoon center during different periods at stations FG, LM, and XF (Fig. 6). In general, lgN_w changed significantly with increasing distance from the typhoon center, while D_0 decreased slightly during the different periods of Typhoon Mangkhut's evolution. Specifically, lgN_w and D_0 at these three stations decreased radially from the typhoon center during the pre-landfall stage, whereas lgN_w increased (decreased) and D_0 decreased slightly during the landfall (post-landfall) stage and radially from the typhoon center, which is different from the results for Typhoon Lekima (Bao et al., 2020b). There may be two reasons for this phenomenon. On the one hand, it could be attributable to the difference in dynamic conditions with radial distance from the typhoon center (Bao et al., 2020a). On the other hand, different microphysical processes, such as accretion forcing and/or coalescence processes below the freezing level could contribute to the DSD discrepancies in the outer rainbands of the same typhoon (Wang et al., 2016; Wen et al., 2018). However, these explanations are hard to verify owing to a lack of observations. Further research is needed.

3.2.2 *Axis ratio*

The raindrop axis ratio obtained from 2DVD observations plays a key role in obtaining the DSR. The raindrop axis ratio is affected by oscillation and tilting effects and varies significantly under different weather conditions. Thus, the resulting axis ratio and DSR should be referred to as the "effective axis" and "effective DSR" (Gorgucci et al., 2000). To show the distribution characteristics, Chang et al. (2009) classified the raindrop axis ratio and diameter as files every 0.02 and 0.20 mm, respectively (Fig. 7). If the number of raindrop particles is less than 10, these particles can be removed to improve the data quality. The results show that the maximum diameter of raindrops during the rainfall process of Typhoon Mangkhut within the study period rarely exceeded 3 mm. Among these, the raindrop size at station LM was generally less than 3 mm, and the number of particles with a diameter larger than 3 mm was the least among the three stations. The number concentration of raindrops with larger drop sizes was also extremely low at station FG.

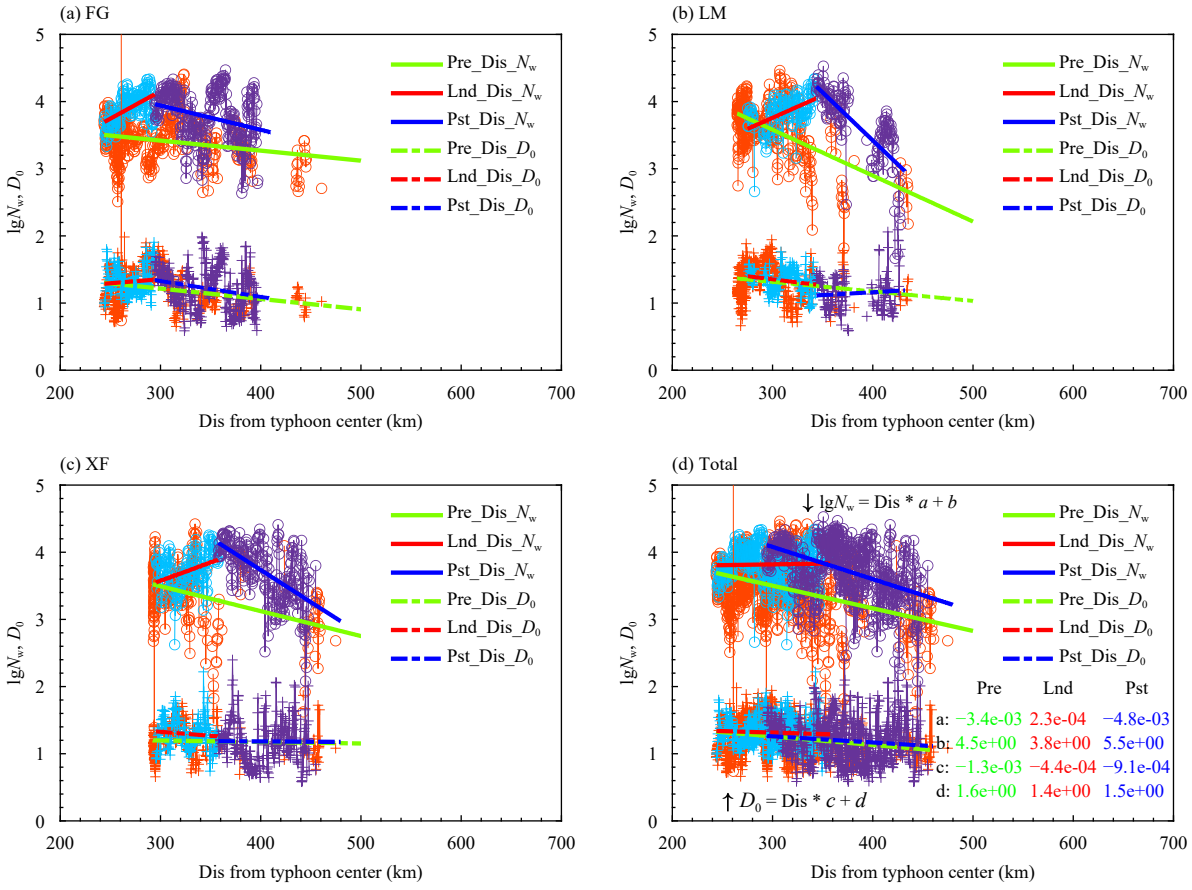

Fig. 6. Scatterplots of lgN_w (upper) and D_0 (lower) versus distance from (a) FG, (b) LM, and (c) XF to the typhoon center during pre-landfall (orange circles), landfall (blue circles), and post-landfall (purple circles). (d) As in (a–c), but for the mean values of lgN_w and D_0 at the three stations. The green, red, and blue solid (dashed) lines denote the lines of best fit for lgN_w (D_0) in different periods. The coefficients for fitting lgN_w–Dis and D_0–Dis are shown in (d).

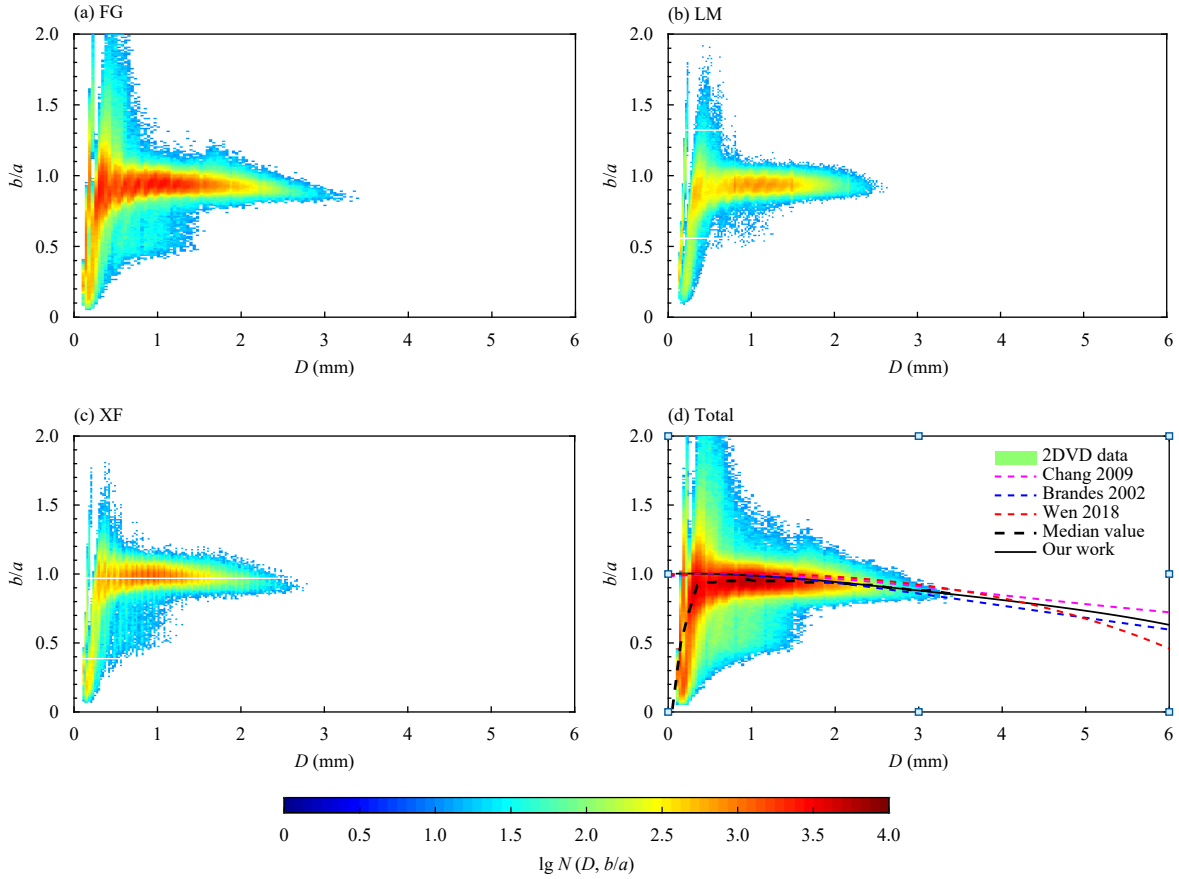

Fig. 7. Distributions of the drop number density [lg$N(D, b/a)$] as a function of drop diameter (D) and axis ratio (b/a) in Mangkhut. (a) FG, (b) LM, (c) XF, and (d) all data. The symbols a and b represent the length of the major and minor axis of raindrops derived from 2DVD, respectively. The black solid line represents the fourth-order fitting of the DSR, and the black dashed line represents the median axis ratio. The pink, blue, and red dashed lines represent the DSR of Chang et al. (2009), Brandes et al. (2002), and Wen et al. (2018), respectively.

Relevant information about the DSR plays a vital role in the process of DSD retrieval by dual-polarimetric radar (Wen et al., 2016). Brandes et al. (2002) combined previous observations to fit a fourth-order polynomial to the raindrop diameter and axis ratio, as shown by the blue dashed line in Fig. 7d. Chang et al. (2009) used 13 typhoon precipitation datasets and reached a conclusion similar to Brandes et al. (2002), as shown by the pink dashed line in Fig. 7d. The curves of Brandes et al. (2002) and Chang et al. (2009) show their strongest similarity when the raindrop diameter is less than 1.5 mm and the raindrop is approximately spherical. When the diameter is more than 1.5 mm, the axis ratio of Chang et al. (2009) is larger and closer to 1, which means that raindrops are closer to a spherical shape. Their results were attributed to the higher wind velocity of the typhoon system, which caused increased vibration and tilting in the raindrops to form nearly spherical shapes. Wen et al. (2018) performed a similar study on seven typhoons that landed in China, as shown by the red dashed line in Fig. 7d. The results of Wen et al. (2018) are closer to the spherical shape than those of Chang et al. (2009), particularly when the diameters are 1.5–3.5 mm, which was attributed to the high horizontal wind speed.

In the present study, performance limitations of the instrument caused a severe deviation in the measured axis ratio of raindrops with diameters < 1.5 mm from the actual axis ratio (Beard et al., 2010). Consequently, axis ratios were artificially set to 0.9999 when diameters were less than 0.7 mm due to the instrumental limitation (Chang et al., 2009). In addition, for drops with diameters ranging from 0.7 to 1.5 mm (Thurai et al., 2007), axis ratios were changed according to the more accurate laboratory measurements of Beard and Kubesh (1991). Considering the data of FG, LM, and XF, the fitted results of the fourth-order polynomial DSR are given in Eq. (14), as represented by the black solid line in Fig. 7d:

$$\frac{b}{a} = -3.478\times10^{-4}D^4 + 4.185\times10^{-3}D^3 - 2.323\times10^{-2}D^2 + 1.040\times10^{-3}D + 1.0017. \quad (14)$$

The coefficient of determination R^2 reaches 0.9741. When the raindrop diameter was less than 1.5 mm, the results of the present study were very close to those in the literature. When the raindrop diameter was 1.5–4 mm, however, our axis ratio results were smaller than those of Chang et al. (2009) and Wen et al. (2018) but slightly larger than that of Brandes et al. (2002). This result is consistent with the findings of Chang et al. (2009) and Wen et al. (2018), in that the high wind velocity in the typhoon caused the raindrop shape to be closer to spherical than that of the raindrops studied by Brandes et al. (2002). When the raindrop diameter was more than 4 mm, our result was slightly smaller than that of Chang et al. (2009) and slightly larger than those of Wen et al. (2018) and Brandes et al. (2002). Before the typhoon landed (0000–0900 UTC 16 September), the average wind velocity ± standard deviation at stations FG, LM, and XF was 8.6 ± 1.9, 9.3 ± 1.9, and 8.9 ± 1.4 m s^{-1}, respectively. After the typhoon made landfall (0900–1600 UTC 16 September), the friction of the land surface caused the wind velocity to drop to 7.3 ± 1.7, 8.2 ± 2.2, and 8.3 ± 1.4 m s^{-1}, respectively. Subsequently, the average wind velocity at all stations further weakened to below 4.0 m s^{-1}, except at XF, as shown by the blue WS curves in Fig. 5. Among the three stations, the wind speed at station XF had the largest average value of 8.2 m s^{-1} during the entire process and the largest axis ratio in diameters of 1–4 mm. With diameters of 1.7–4 mm, the axis ratio at station LM was greater than that at station FG. The average wind velocity at the latter site, at 7.3 m s^{-1}, was smaller than that at the former site, at 8.2 m s^{-1} in the landfall stage. Excellent correspondence was observed between the high wind speed and large axis ratio, which also verifies the inference of Chang et al. (2009) and Wen et al. (2018). Since no exact wind velocity information was provided by Chang et al. (2009) and Wen et al. (2018), a comparison cannot be made between our work and theirs. However, referring to the discussion above, the difference in wind velocity may explain why the raindrop shape in the present study was closer to an ellipsoid than those of Chang et al. (2009) and Wen et al. (2018).

3.3 *Classification of precipitation types and corresponding normalized DSDs*

In the study of DSD, N_w and D_0 play important roles, particularly in improving GPM/DPR (Ji et al., 2019). In the present study, D_0 and $\lg N_w$ are divided into 40 parts from 0–3.5 mm and 1–5.5 mm^{-1} m^{-3} to show the distribution of raindrop particles, respectively. Drops with $\lg N_w$ of 1.0–1.5 mm^{-1} m^{-3} and D_0 of 3.4–4.3 mm appear more frequently. The blue dashed lines in Figs. 8a–c separate the CR and SR types based on the study of Bringi et al. (2009), hereinafter referred to as BR09, as shown in Eq. (15):

$$\lg N_w^{sep} = c_1 D_0 + c_2, \tag{15}$$

where c_1 and c_2 are usually equal to −1.6 and 6.3, respectively. According to this classification method, N_w–D_0 pairs above (below) Eq. (15) in the figure are recognized as CR (SR). In general, SR accounts for 90.53%. The rain type at station FG was mainly stratiform, at 88.4%, with CR accounting for 11.6%. At station LM, most drops were located below the blue dashed line, with CR accounting for 10.8%. A process of evolution between SR and CR was noted. The drops observed at station XF were mostly SR, at 93.8%, and the proportion of convective precipitation drops was the least at this site, at 6.2%. The classification results show that the proportion of SR may be significantly overestimated at each station because the separator line of BR09 is set based on monsoon precipitation and is not appropriate for fast-moving typhoon rainband precipitation.

Considering the fast passage of convective typhoon rainbands over the disdrometer and the low R of SR in the outer area, Bao et al. (2019) established a method that is more suitable for the classification of typhoon precipitation than the methods of Testud et al. (2001), Bringi et al. (2003), and Chen et al. (2012). The method of Bao et al. (2019), hereinafter referred to as BA19, proposed that (1) if all adjacent R values from R_{k-5} to R_{k+5} are higher than 0.1 mm h^{-1} and less than 5.0 mm h^{-1} and the standard deviation (R_{k-5} to R_{k+5}) is less than 1.5 mm h^{-1}, the spectrum k is classified as SR; (2) if the R values from R_{k-5} to R_{k+5} are higher than 0.1 mm h^{-1}, the mean value of R_{k-5} to R_{k+5} is higher than 5.0 mm h^{-1} and the standard deviation (R_{k-5} to R_{k+5}) is higher than 1.5 mm h^{-1}, and three adjacent R values (R_{k-1} to R_{k+1}) are higher than 5.0 mm h^{-1}, the spectrum k is classified as CR; and (3) the remaining samples are considered as mixed rain.

The rain types of CR and SR at the three stations are classified in Figs. 8d–f using 1-min R data after quality control. At station FG, there were 292 (32.5%) and 151 (16.8%) samples out of a total of 898 samples that were classified as SR and CR, respectively. Most of the samples were mixed rain (50.7%); 118 (16.4%) and 138 (19.2%) of 718 samples were considered as SR and CR at station LM; and 223 (29.5%) and 46 (6.1%) of 756 samples were SR and CR at station XF.

The method of BR09 does not consider the existence of mixed rain, which increases the proportion of SR. Moreover, there is a sharp separator line between the SR

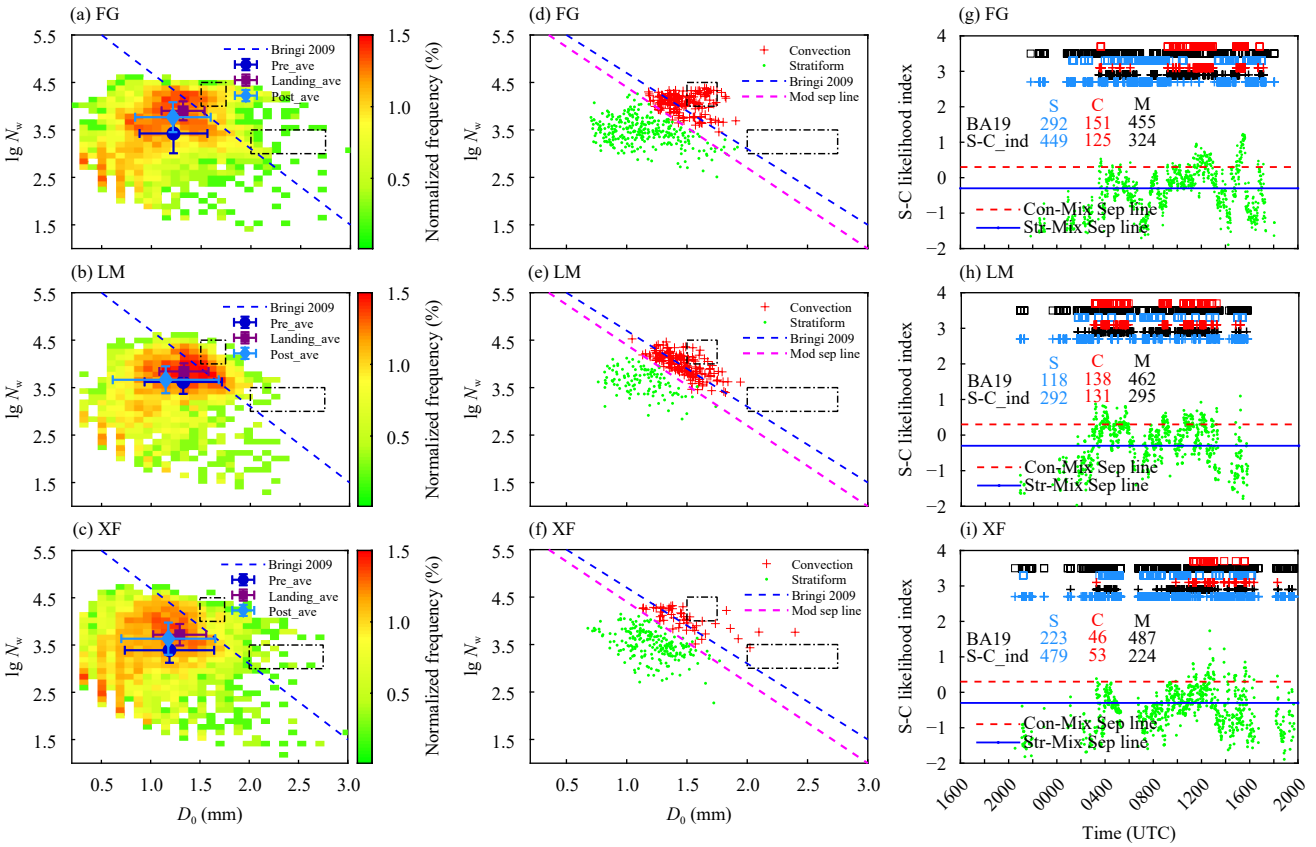

Fig. 8. Normalized occurrence frequency (color-shaded) and scatterplots of D_0 versus lgN_w. (a) Stations FG, (b) LM, and (c) XF. The blue dashed line represents the stratiform/convective separation line from BR09. Panels (d), (e), and (f) are scatterplots using the method of BA19, in which green dots denote SR and red plus signs denote CR (mixed rain type excluded), recorded at stations FG, LM, and XF, respectively. The magenta oblique dashed line represents the modified stratiform/convective separation line based on the rain type classification results of the BA19 method. Panels (g), (h), and (i) compare the precipitation classification results using the S–C likelihood index (plus signs) and BA19 (squares) method. Blue, red, and black symbols indicate stratiform, convective, and mixed rain, respectively. Green dots represent the S–C likelihood index (i) ($i > 0.3$ for CR; $-0.3 \leqslant i \leqslant 0.3$ for mixed or transitional rain; $i < -0.3$ for SR).

and CR scatters, which is approximately parallel to the line of BR09. Thus, a modified separator line was drawn after visual inspection of BA19 precipitation classification datasets, as shown by the magenta dashed line in Figs. 8d–f. Here, the values of c_1 and c_2 in Eq. (15) are modified to −1.7 and 6.1 to adapt to the typhoon precipitation. The value of c_1 is within the recommended range (−1.6 to −1.7) of BR09 and Thurai et al. (2010), while c_2 is lower than the corresponding value range (6.3 to 6.4), which is related to the threshold of the CR rate in different classification methods. The threshold value of the CR rate in the BA19 method is 5.0 mm h^{-1}, while a similar value in the BR09 and Testud et al. (2001) methods is set to 10.0 mm h^{-1}. In addition, the sensitivity of c_2 to the CR intensity threshold is verified.

In order to make the classification of rain type more visual and direct based on the modified separator line, a rain type "S–C likelihood index" (denoted by "i") is introduced (Thurai et al., 2016), given by

$$i = \lg N_w - \lg N_w^{sep}. \quad (16)$$

CR is indicated when $i > 0.3$, SR when $i < -0.3$, and mixed/transitional rain when $-0.3 \leqslant i \leqslant 0.3$. According to the rain type classification results of the three stations in Figs. 8g–i, the S–C likelihood index (green dots) can continuously and clearly represent the evolution of different rain types (stratiform/convective/mixed or transitional) in the typhoon precipitation, combined with the red and blue dividing lines. The classification results of BA19 (squares) and modified S–C likelihood index (plus signs) are placed in the upper right of Figs. 8g–i (blue, red, and black markers indicate stratiform, convective and mixed or transitional rain, respectively), from which we can see that the two methods have excellent consistency in their classification of CR, whereas the classification of stratiform and mixed (or transitional) rain is easily confused, possibly due to the different microphysical processes, which will be further analyzed and verified by using dual-polarization radar echo data in the future.

Chen et al. (2012) reported that collision and coalescence of raindrops are usually the main source of CR in typhoon precipitation and that the raindrops of SR are formed by melting and aggregation of graupel and ice particles. Bringi et al. (2003) found that the change in N_w–D_m reflects the difference in different microphysical processes in SR. Large D_m and small N_w values might be caused by large particles of dry snow melting, whereas small D_m and large N_w could originate from the melting of small graupel or ice particles. In Typhoon Mangkhut, the D_m of most of the SR was relatively small, and N_w was relatively large. This phenomenon indicates that the SR in this typhoon could have originated from small and dense graupel particles or ice crystals rather than from large particles of low-density dry snow. This finding is essentially consistent with the results of Wen et al. (2018), who analyzed the microphysical processes of precipitation in Typhoon Matmo in 2014. Bringi et al. (2003) reported that the ranges of D_0 and lgN_w in maritime (continental) convection are roughly 1.5–1.75 (2–2.75) mm and 4–4.5 (3–3.5) mm^{-1} m^{-3}, respectively, as indicated by the two outlined squares in Fig. 8. According to the lgN_w–D_m distribution, the three sites overlapped with maritime convection to a greater extent, and the proportion of continental convection was relatively small. Wang et al. (2016) studied the microphysical characteristics of precipitation during Typhoon Matmo near Nanjing in 2014. In their study, a 2DVD was deployed 101–170 km away from the center of Matmo after it made landfall, whereas Mangkhut was more than 275 km away from LM after it made landfall. In Wang et al. (2016), D_m and lgN_w were 1.41 mm and 4.67 mm^{-1} m^{-3}, respectively, which is 0.17 mm and 0.78 mm^{-1} m^{-3} higher, respectively, than that at station LM. Bao et al. (2020a) found that the fact that N_w (D_m) increases as distance increases (decreases) could be related to dynamic factors such as updraft motion. Wang et al. (2016) attributed the radial distribution discrepancy to the environmental humidity and topographic forcing. As is shown in Fig. 6, lgN_w–Dis and D_0–Dis tend to exhibit various relationships in different stages. For comparison, the values of D_0 and lgN_w were estimated at radii of 110, 140, and 170 km from Mangkhut during its landfall and post-landfall stages. The average values of lgN_w (D_0) were approximately 4.29 (1.53), 4.23 (1.49), and 4.16 (1.46) at the three radii, respectively, which are much closer to the results of Wang et al. (2016). Therefore, it can be inferred that the relative distance between the station and the typhoon center might be a reason for the inhomogeneous radial distribution of the raindrop number concentration.

On the basis of the method of BA19, precipitation can be classified into SR and CR. Fig. 9 shows scatterplots of the scaled DSD $N(D)/N_w$ and the normalized diameter parameter D/D_0 of the SR and CR at the three sites where the 2DVDs were located. The black dashed lines indicate the normalized gamma distribution for μ of SR (CR) between 0 (−1) and +3 (+2). The brown solid lines indicate the normalized gamma distribution from the μ search method (Testud et al., 2001; Bringi et al., 2003), which searches for μ by minimizing the absolute deviation between the measured normalized DSD data and the normalized gamma distribution using the following expression:

$$\mu_s = \min\left\{\sum_{i=1}^{41} \mathrm{abs}[\lg N_{obs}(D_i) - \lg N_{model}(D_i)]\right\}. \quad (17)$$

The normalized gamma distribution enables a comparison of the DSD of different R values by using the normalized diameter parameter D/D_0 and N_w (Bringi et al., 2003). The results demonstrate that the values of μ are different for SR and CR. A comparison of the SR and CR at the same location revealed a smaller corresponding μ of the CR. In addition, the normalized diameter parameter D/D_0 was almost always less than 2.5, regardless of the rain type. In the SR, the three stations showed strong downward curves at the small-diameter end. In the CR, however, the degree of curvature was not strong, which is consistent with the conclusions of Zhang et al. (2017). Regardless of the rain type, station LM (XF) had the largest (smallest) μ, with values of 1.98 and 0.82 (1.32 and 0.38) for SR and CR, respectively. This phenomenon means that the distribution curve for station LM was more curved at the small-diameter end. For raindrops with diameters of 0–0.5 mm, the number concentration at station LM (XF) was relatively small (large).

3.4 *GPM improvement*

Although some regions of the world have a sufficient density of rain gauges and radars to measure precipitation, less populated regions, such as ocean areas and some developing countries, still lack measurement facilities (Kidd et al., 2017). Satellites can make up for such shortcomings of precipitation observation. GPM/DPR rainfall retrieval algorithms use the normalized gamma distribution as shown in Eq. (6) to describe the DSD (Chen et al., 2017). The normalized DSD model enables comparison of the DSD regardless of the time scale and R, and accurately examines the substantial variations that are related to the physical rainfall regimes (Zhang et al., 2017). GPM/DPR consists of Ka-band and Ku-band radar. After a relationship between the radar reflectivity in the Ka band (Z_{Ka}), Ku band (Z_{Ku}), and N_w, D_0 is estab-

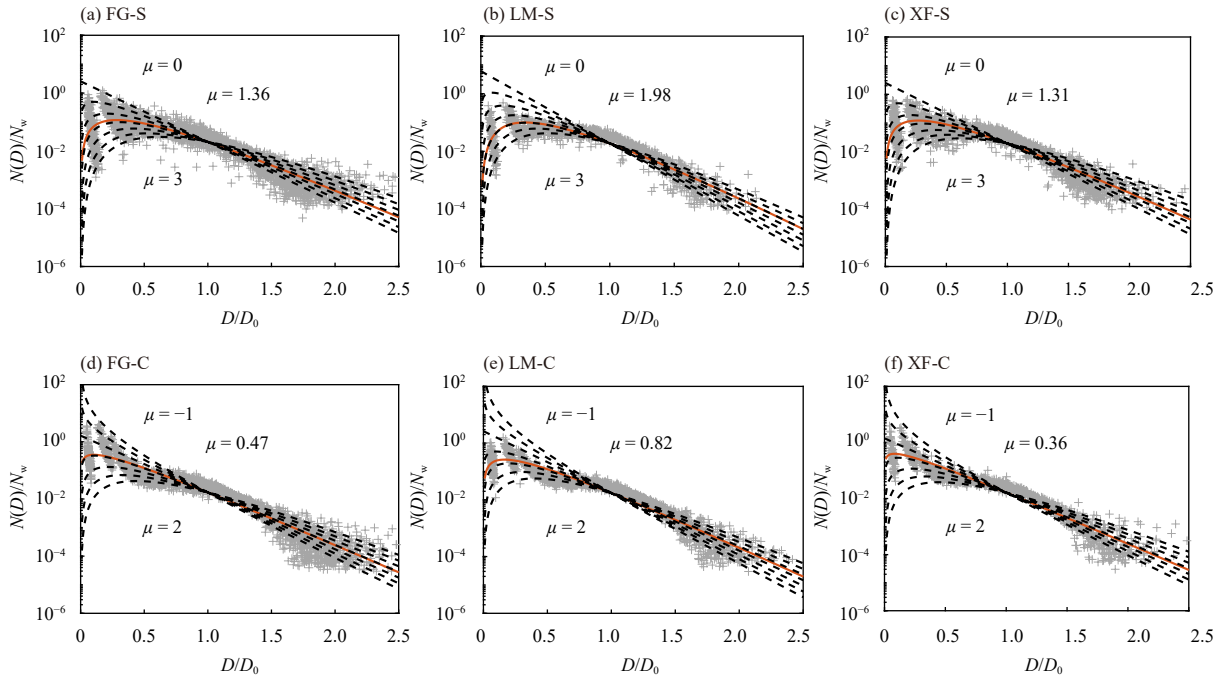

Fig. 9. Scatterplots of scaled DSD $N(D)/N_w$ and the normalized diameter parameter D/D_0 of the SR and CR. The black dashed lines indicate the normalized gamma distribution for μ of SR (CR) between 0 (−1) and +3 (+2), and the brown solid lines indicate the normalized gamma distribution from the μ search method. The SR and CR regions for stations (a, d) FG, (b, e) LM, and (c, f) XF are shown, respectively.

lished, and satellites can retrieve N_w and D_0 using Z_{Ka} and Z_{Ku}. The DSD can be obtained based on the normalized gamma distribution with a given μ, and then R is calculated (Wu et al., 2019). The effective radar reflectivity factor Z_e at a specific wavelength can be expressed as

$$Z_e = \frac{\lambda^4}{\pi^5 |K_w|^2} \sum_{i=1}^{n} N(D_i)\sigma_b(D_i,\lambda)\Delta D_i, \qquad (18)$$

where λ represents the radar wavelength, $|K_w|^2$ is the dielectric factor of water and is conventionally taken to be 0.93, σ_b is the backscattering cross-section of a raindrop with diameter D_i, and n is the total number of bins.

Figures 10a and 10b show D_0–Z_{Ku} and D_0–Z_{Ka} scatterplots, respectively. The retrieved Z_{Ku} and Z_{Ka} are mainly distributed in the range from 10 to 40 dBZ. In this work, D_0 and Z_{Ku} are fitted with second-order polynomials based on the least-square method. The corresponding results are shown in Table 3.

The fitted curves show excellent agreement with the scatterplots, with R^2 values of 0.71, 0.70, and 0.74 for SR, CR, and total samples, respectively. Chen et al. (2017), hereinafter referred to as CH17, used a similar method to fit D_m–Z_{Ku} (Fig. 10a, red solid line). Wu et al. (2019), hereinafter referred to as WU19, applied a second-order polynomials regression model to fit the precipitation datasets in Northwest Pacific (Fig. 10a, green solid line). For a gamma distribution, D_0 can be expressed in terms of D_m [$D_0 = (3.67 + \mu) / (4 + \mu)D_m$], and D_m is a reasonable approximation for D_0 for all $\mu > -2$ (Ulbrich, 1983). In this work, D_0, which is physically as meaningful as D_m (Testud et al., 2001), is substituted for D_m when plotting the curves in Fig. 10. Figure 10a compares the fitted result of our research with that of CH17 and WU19. For $Z_{Ku} < 37$ (> 37) dBZ, D_0 is larger (smaller) than that of CH17. However, D_0 is larger (smaller) than that of WU19 when $Z_{Ku} < 14$ (> 14) dBZ.

The same process was applied to D_0–Z_{Ka}, and its distribution was found to be similar to that of D_0–Z_{Ku} (Fig. 10b). The fitted results are shown in Table 3, with R^2 values of 0.69, 0.51, and 0.70 for SR, CR, and total samples, respectively. For $Z_{Ka} < 35$ (> 35) dBZ, D_0 is larger (smaller) than that of CH17. However, D_0 is smaller than that of WU19.

To obtain a more accurate relationship between $\lg N_w$ and D_0, the samples with $R < 1$ mm h^{-1} were excluded. Based on the classification scheme of BA19, second-order polynomial fitting was applied to $\lg N_w$–D_0 in terms of SR and CR. The results are shown in Table 3.

Figure 11 presents scatterplots of $\lg N_w$–D_0 in terms of SR and CR at the three stations, in addition to a kernel density plot, which is a non-parametric way of estimating the probability density function of a random variable. Fitting was applied to $\lg N_w$–D_0 according to SR (R^2 =

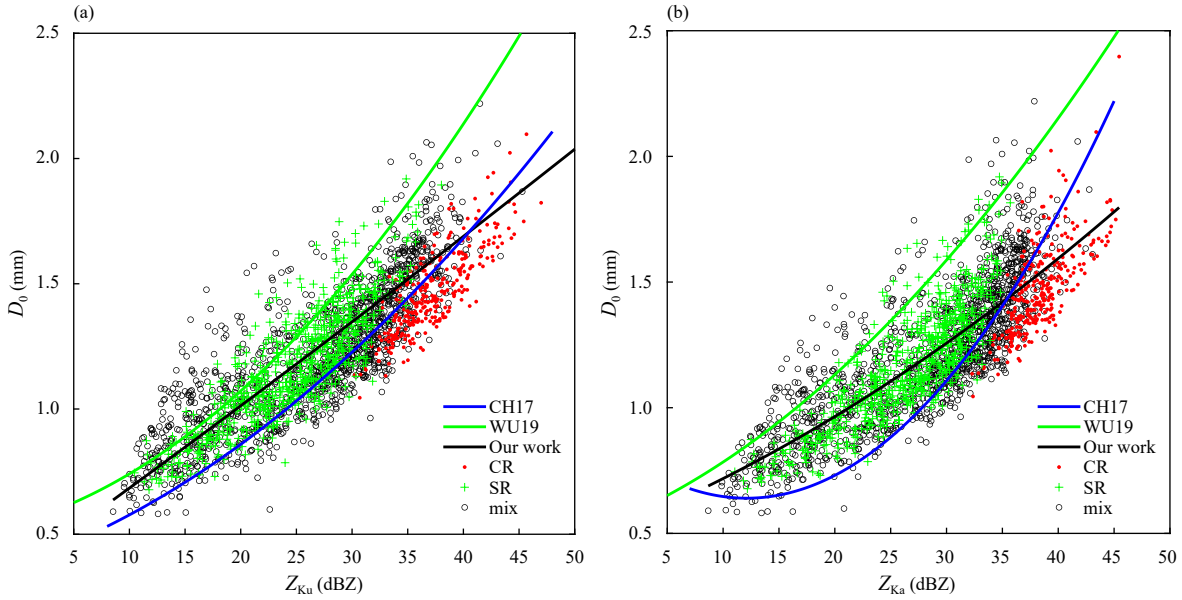

Fig. 10. Scatterplots of (a) D_0–Z_{Ku} and (b) D_0–Z_{Ka}. The open circles, red dots, and green plus signs represent the D_0–Z_{Ku}(Z_{Ka}) of mixed rain, CR, and SR, respectively. The black solid lines are the lines of best fit for all data. The blue and green solid lines are the fitted curves of CH17 and WU19, respectively.

Table 3. Second-order polynomial relations of D_0–Z_{Ku}, D_0–Z_{Ka}, and N_w–D_0 for CR and SR

Relation	Data	α	β	γ
$D_0 = \alpha Z_{Ku}^2 + \beta Z_{Ku} + \gamma$	SR	0.0005171	0.01162	0.5551
	CR	0.0006511	−0.004165	0.7142
	Total	0.00024857	0.0171	0.5612
$D_0 = \alpha Z_{Ka}^2 + \beta Z_{Ka} + \gamma$	SR	0.0007447	−0.0004788	0.6487
	CR	−0.0009987	0.1293	−2.012
	Total	0.000238	0.0175	0.5152
$\lg N_w = \alpha D_0^2 + \beta D_0 + \gamma$	SR	−0.7395	1.2310	3.1490
	CR	0.2570	−1.532	5.7250
	Total	−0.1746	−0.0751	4.195

0.26) and CR (R^2 = 0.37), respectively, and showed a discernible difference. However, in terms of $\lg N_w$–D_0 for all samples, the fitting was generally poor (R^2 = 0.16), which shows the need for rain type classification in GPM. The $\lg N_w$–D_0 curve of CR is located above the SR curve and the curves are approximately parallel. However, the fitted result of the combination of SR and CR was relatively poor (R^2 = 0.15), which implies that SR and CR should be separated when discussing $\lg N_w$–D_0 relationships. The results of CH17 (black solid line) and WU19 (pink solid line) were compared to the current study. The curve obtained by WU19 deviates significantly from the observed data and is inapplicable to Typhoon Mangkhut. CH17 is close to the fitted curve of SR, but inapplicable to CR. Overall, by combining the D_0–Z_{Ku}, D_0–Z_{Ka}, and $\lg N_w$–D_0 relations, the DSD can be obtained based on the normalized gamma distribution with a given μ. Consequently, R can be derived through GPM/DPR. This study may help expand the GPM algorithm and improve the accuracy of rainfall retrieval in typhoon precipitation in South China.

3.5 *QPE*

The present study used three radar parameters (Z_h, Z_{DR}, and K_{DP}) and R to establish a relationship for using radar to estimate the precipitation. During the landfall of Typhoon Mangkhut, station FG (XF) was closest to (farthest from) the typhoon. Therefore, the data of these stations were combined as a training set to fit R and Z_h, K_{DP}, and Z_{DR} to make the data more representative. The following four relationships used by Ji et al. (2019) are given to fit the parameters:

$$R_{dpr}(Z_h, Z_{DR}) = \delta Z_h^{\varepsilon} 10^{\zeta Z_{DR}}, \tag{19}$$

$$R_{dpr}(K_{DP}, Z_{DR}) = \delta K_{DP}^{\varepsilon} 10^{\zeta Z_{DR}}, \tag{20}$$

$$R_{dpr}(K_{DP}) = \delta K_{DP}^{\varepsilon}, \tag{21}$$

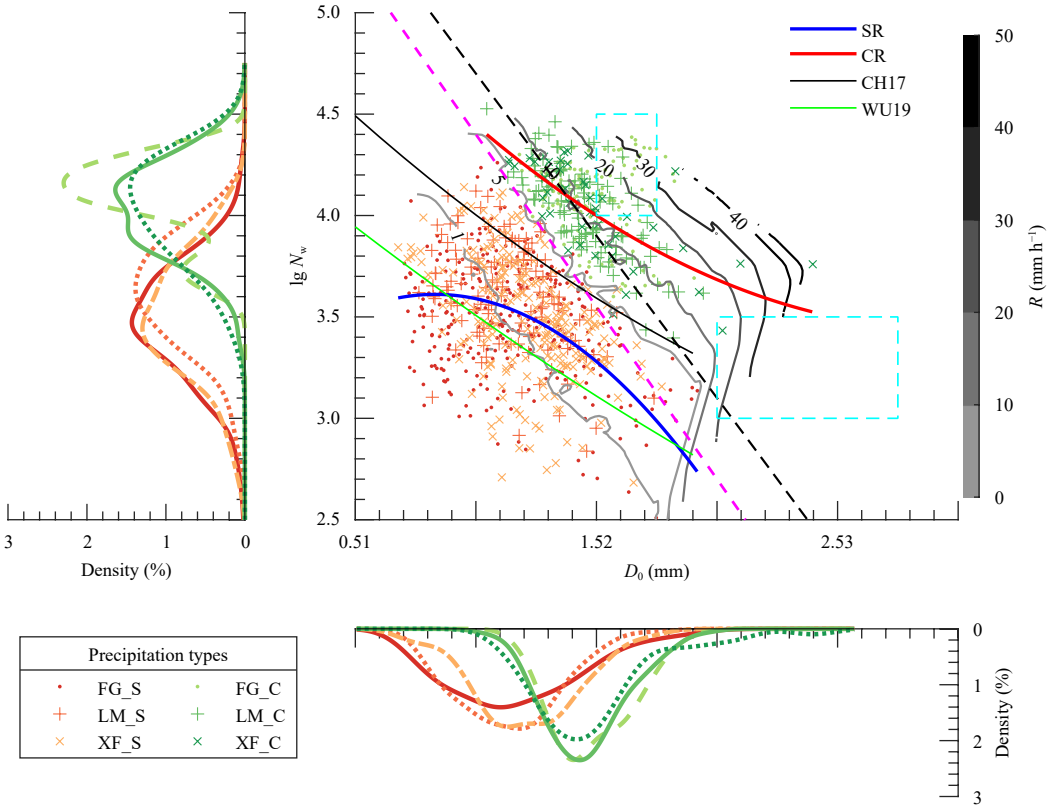

Fig. 11. Scatterplots of lgN_w–D_0 for SR and CR at three stations (top-right panel) along with the corresponding kernel density plots (bottom and top-left panels). The blue and red solid lines represent the fitted curves of SR and CR, respectively. The black and green solid lines are the fitted curves obtained by the methods of CH17 and WU19. The SR/CR separation scheme of BR09 and the modified separator line are drawn as the black and magenta dashed line, respectively. Light green (orange) dotted, green (orange) solid, and dark green (orange) dashed curves in each kernel density plot indicate the distributions of lgN_w and D_0 at FG, LM, and XF for SR (CR), respectively. The gray contours represent the distribution of R.

$$R_{\mathrm{dpr}}(Z_{\mathrm{h}}) = \delta Z_{\mathrm{h}}^{\varepsilon}, \tag{22}$$

where δ, ε, and ζ are the coefficients in each relational expression. The coefficients in this study are shown in Table 4.

The coefficient δ in R_{dpr} (K_{DP}, Z_{DR}) and R_{dpr} (K_{DP}) was three to four times larger than that obtained by Ji et al. (2019); only negligible differences were noted in the other coefficients. To explore the accuracy and validity of the QPE relational formulae, they were applied to the station LM data, and the consistency between the measured and estimated R of station LM was examined. The following evaluation indices were used to quantitatively describe the validity of the formula: root-mean-square deviation (RMSD), R^2, and the index of agreement d_{r}, the latter of which is a dimensionless evaluation index used for evaluating model performance, with −1.0 and +1.0 given as the boundaries. This index is eminently flexible and applicable to various model performance evaluation problems (Willmott et al., 2012). RMSD and d_{r} can be expressed as

$$\mathrm{RMSD} = \sqrt{\frac{\sum_{i=1}^{N}(y_i - x_i)^2}{N}} \tag{23}$$

and

$$d_{\mathrm{r}} = \begin{cases} 1 - \dfrac{\sum_{i=1}^{N}|x_i - y_i|}{c\sum_{i=1}^{N}|y_i - \overline{y_i}|}, \text{when} & \sum_{i=1}^{N}|x_i - y_i| \leqslant c\sum_{i=1}^{N}|y_i - \overline{y_i}| \\ \dfrac{c\sum_{i=1}^{N}|y_i - \overline{y_i}|}{\sum_{i=1}^{N}|x_i - y_i|} - 1, \text{when} & \sum_{i=1}^{N}|x_i - y_i| > c\sum_{i=1}^{N}|y_i - \overline{y_i}| \end{cases}, \tag{24}$$

where x_i is the result estimated by the QPE formula, y_i is the actual observation result, N is the data length, and c is 2. The estimated and observed results are substituted into the formula to obtain the results shown in Table 5.

The three evaluation indexes of R_{dpr}(K_{DP}, Z_{DR}) are the best, regardless of rain type, followed by R_{dpr}(Z_{h}, Z_{DR}),

Table 4. QPE formula coefficients for stations FG and XF with combined data fits for total samples/CR/SR

Parameter	$R_{dpr}(Z_h, Z_{DR})$	$R_{dpr}(K_{DP}, Z_{DR})$	$R_{dpr}(K_{DP})$	$R_{dpr}(Z_h)$
δ	0.008/0.009/0.012	99.237/92.612/119.567	57.552/57.619/32.289	0.029/0.055/0.040
ε	0.908/0.882/0.899	0.922/0.904/0.894	0.800/0.766/0.699	0.682/0.626/0.585
ζ	−0.428/−0.382/−0.744	−0.204/−0.175/−0.468	---	---

Table 5. Evaluation index values of the estimated R for total rain samples/CR/SR using four QPE formulae

Parameter	$R_{dpr}(Z_h, Z_{DR})$	$R_{dpr}(K_{DP}, Z_{DR})$	$R_{dpr}(K_{DP})$	$R_{dpr}(Z_h)$
RMSD	0.806/1.561/0.179	0.677/1.229/0.179	1.162/2.147/0.326	1.925/3.625/0.425
R^2	0.990/0.989/0.973	0.993/0.974/0.973	0.979/0.979/0.910	0.943/0.939/0.848
d_r	0.941/0.836/0.915	0.944/0.856/0.909	0.921/0.774/0.873	0.891/0.674/0.836

$R_{dpr}(K_{DP})$, and $R_{dpr}(Z_h)$. Obviously, $R_{dpr}(K_{DP}, Z_{DR})$ and $R_{dpr}(Z_h, Z_{DR})$, which combine multiple parameters, perform better than $R_{dpr}(K_{DP})$ and $R_{dpr}(Z_h)$, and $R_{dpr}(K_{DP})$ is superior to $R_{dpr}(Z_h)$. The two formulae relate to K_{DP} performed better, which might be attributable to the fact that K_{DP} is immune to the absolute calibration error or attenuation effect. It is unbiased if rain is mixed with spherical hail (Bringi and Chandrasekar, 2001). Moreover, K_{DP} is insensitive to the variation of D_m and D_0, making $R_{dpr}(K_{DP}, Z_{DR})$ more independent of the variation of DSD.

The QPE formulae have obvious regional differences, and the corresponding formulae for precipitation related to different systems can also differ. Figure 12 shows Taylor diagrams based on the QPE formulae obtained by various scholars for different regions and precipitation systems. In addition, R calculated by the formula is compared with the measured R at station LM.

The correlation for each formula is above 0.95, with the differences manifested mainly in the different standard deviations. The points in Figs. 12b and 12c are distant from the observation point, and the distribution is scattered probably because the correspondence between K_{DP} and R in different regions and precipitation systems

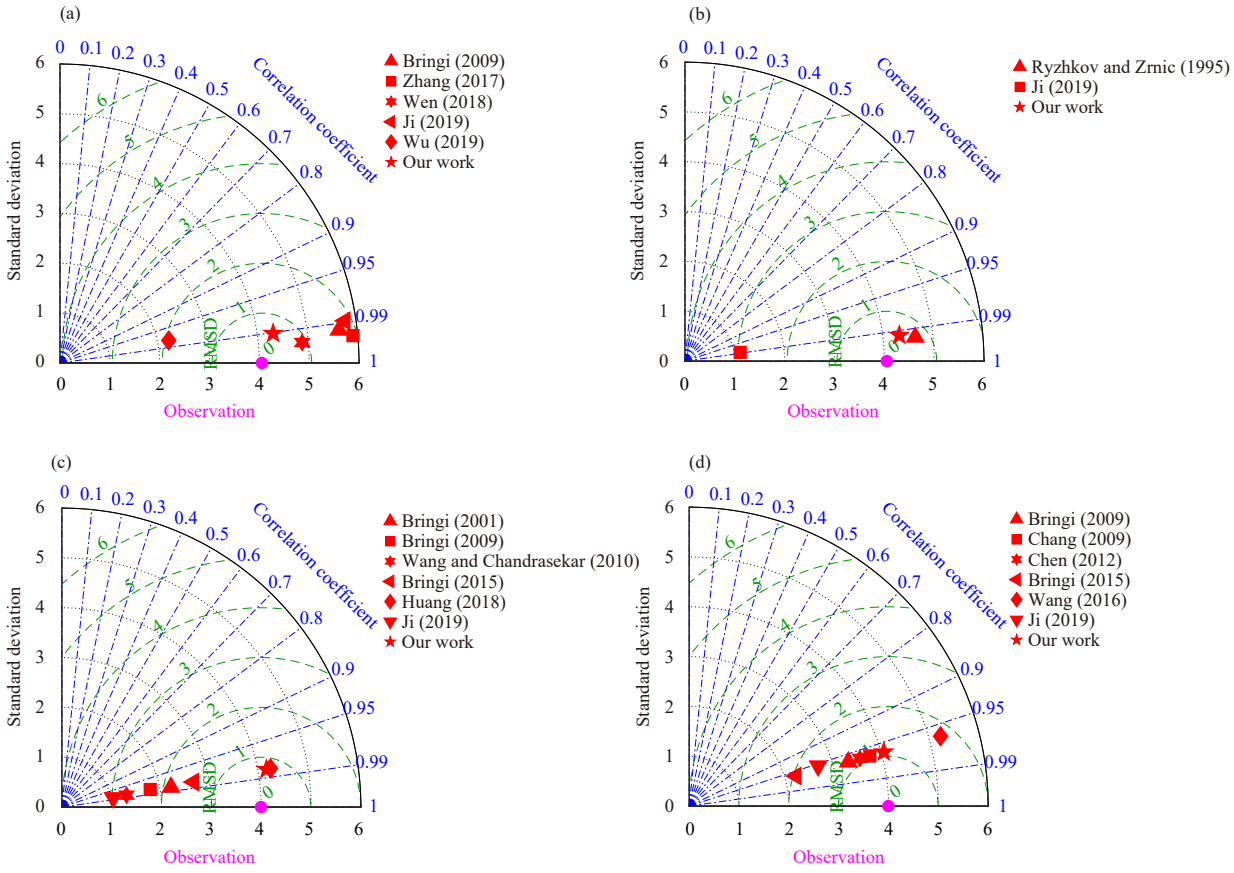

Fig. 12. Taylor diagrams showing the index of agreement, standard deviation, and RMSD for the four formulae: (a) $R_{dpr}(Z_h, Z_{DR})$, (b) $R_{dpr}(K_{DP}, Z_{DR})$, (c) $R_{dpr}(K_{DP})$, and (d) $R_{dpr}(Z_h)$.

is quite different. This K_{DP}-based QPE method is more accurate than other parameters for specific regions and specific precipitation systems, although it is sensitive to changes in these factors. Figure 12d shows the results of $R_{dpr}(Z_h)$, in which each point is closer to the observation point. The performance of $R_{dpr}(Z_h)$ in evaluating precipitation is inferior to that of $R_{dpr}(K_{DP}, Z_{DR})$ (with similar standard deviation but higher RMSD and a lower correlation coefficient), although the former is obviously more universal.

4. Conclusions

The present study employed DSD and axis ratio data at stations FG, LM, and XF on 15–16 September 2018 and investigated the microphysical characteristics of precipitation in the outer rainbands of Typhoon Mangkhut. The main conclusions can be summarized as follows:

(1) Significant temporal and spatial differences were noted in the microphysical characteristics of precipitation in the outer rainbands of Typhoon Mangkhut. Raindrops with a diameter < 3 mm accounted for more than 99% of the total precipitation. The strongest rainfall was recorded at 1550, 1300, and 1300 UTC 16 September at stations FG, LM, and XF, respectively. It is noted that $\lg N_w$ and D_0 decreased radially from the typhoon center during the pre-landfall stage. However, $\lg N_w$ increased (decreased), and D_0 decreased slightly, during the landfall (post-landfall) stage, without consistent change in these two parameters in different stages of the typhoon (Bao et al., 2020b).

(2) According to the axis ratio of the entire precipitation process, the shapes of raindrops in Typhoon Mangkhut with diameters of 1.5–4 mm were more elliptical than those reported by Wen et al. (2018) and Chang et al. (2009), but were closer to spherical than the results of Brandes et al. (2002). The variation in raindrop shapes can be attributed to the differences in wind power in the precipitation system. For raindrops with diameters < 1.5 mm, the results of the present study are comparable to those of previous studies in terms of the shape of raindrops. The raindrops with diameters > 4 mm in the present study were closer to ellipsoid than those of Chang et al. (2009), and closer to spherical than those of Wen et al. (2018) and Brandes et al. (2002).

(3) A modified separator line for SR and CR was derived based on the work of BA19 using N_w and D_0 scatterplots. This new classification scheme was compared to the method of BA19 by applying the S–C likelihood index (Thurai et al., 2016). The two classification schemes showed high consistency in terms of separating CR, but conformed poorly to SR and mixed rain. Based on the method of BA19, 32.5% (16.8%), 16.4% (19.2%) and 29.5% (6.1%) of samples were classified as SR (CR) at stations FG, LM, and XF, respectively. A comparison of the SR and CR at a single location revealed that the corresponding μ of the CR was relatively small and that the normalized gamma distribution fitted curve of the SR was more severely curved in the small particle-size section. Moreover, the SR may have originated mainly from small and dense graupel particles or ice crystals.

(4) In order to improve the inversion accuracy of the normalized gamma distribution, we calculated Z_e in the Ku and Ka bands and derived the empirical relations of D_0–Z_e. The variable D_0 was also fitted to N_w according to SR and CR, separately. Compared to the results of CH17 and WU19, our relationships are more suitable for GPM DPR rainfall retrieval in the outer rainbands of typhoons in South China. The estimated result of $R_{dpr}(K_{DP}, Z_{DR})$ matched the measured data best for all three types of precipitation, although the retrievals can be more sensitive to changes in K_{DP}. The retrievals of the traditional $R_{dpr}(Z_h)$ relationship, i.e., the Z–R relationship, were less favorable than the fitted results by combining K_{DP} and Z_{DR}. However, $R_{dpr}(Z_h)$ showed broader applicability.

Acknowledgments. Thanks are given to Tengfei Zheng from the Guangzhou Institute of Tropical and Marine Meteorology of China Meteorological Administration for help in processing the observations of the two-dimensional video disdrometer (2DVD). We are also grateful to Qin Huang from the University of Auckland for invaluable assistance throughout the preparation of the original manuscript. Finally, we thank the Editor and all anonymous reviewers for their valuable suggestions that have helped improve this paper.

REFERENCES

Bao, X. W., L. G. Wu, B. Tang, et al., 2019: Variable raindrop size distributions in different rainbands associated with Typhoon Fitow (2013). *J. Geophys. Res. Atmos.*, **124**, 12,262–12,281, doi: 10.1029/2019JD030268.

Bao, X. W., L. G. Wu, S. Zhang, et al., 2020a: Distinct raindrop size distributions of convective inner- and outer-rainband rain in Typhoon Maria (2018). *J. Geophys. Res. Atmos.*, **125**, e2020JD032482, doi: 10.1029/2020JD032482.

Bao, X. W., L. G. Wu, S. Zhang, et al., 2020b: A comparison of convective raindrop size distributions in the eyewall and spiral rainbands of Typhoon Lekima (2019). *Geophys. Res. Lett.*, **47**, e2020GL090729, doi: 10.1029/2020GL090729.

Beard, K. V., and R. J. Kubesh, 1991: Laboratory measurements of small raindrop distortion. Part 2: Oscillation frequencies and modes. *J. Atmos. Sci.*, **48**, 2245–2264, doi: 10.1175/1520-0469(1991)048<2245:Lmosrd>2.0.Co;2.

Beard, K. V., V. N. Bringi, and M. Thurai, 2010: A new understanding of raindrop shape. *Atmos. Res.*, **97**, 396–415, doi: 10.1016/j.atmosres.2010.02.001.

Brandes, E. A., G. F. Zhang, and J. Vivekanandan, 2002: Experiments in rainfall estimation with a polarimetric radar in a subtropical environment. *J. Appl. Meteor.*, **41**, 674–685, doi: 10.1175/1520-0450(2002)041<0674:EIREWA>2.0.CO;2.

Bringi, V. N., and V. Chandrasekar, 2001: *Polarimetric Doppler Weather Radar: Principles and Applications*. Cambridge University Press, Cambridge, 664 pp.

Bringi, V. N., V. Chandrasekar, J. Hubbert, et al., 2003: Raindrop size distribution in different climatic regimes from disdrometer and dual-polarized radar analysis. *J. Atmos. Sci.*, **60**, 354–365, doi: 10.1175/1520-0469(2003)060<0354:rsdidc>2.0.co;2.

Bringi, V. N., C. R. Williams, M. Thurai, et al., 2009: Using dual-polarized radar and dual-frequency profiler for DSD characterization: A case study from Darwin, Australia. *J. Atmos. Oceanic Technol.*, **26**, 2107–2122, doi: 10.1175/2009JTECHA1258.1.

Cao, Q., G. F. Zhang, E. Brandes, et al., 2008: Analysis of video disdrometer and polarimetric radar data to characterize rain microphysics in Oklahoma. *J. Appl. Meteor. Climatol.*, **47**, 2238–2255, doi: 10.1175/2008jamc1732.1.

Cao, Q., M. B. Yeary, and G. F. Zhang, 2012: Efficient ways to learn weather radar polarimetry. *IEEE Trans. Educ.*, **55**, 58–68, doi: 10.1109/te.2011.2118211.

Chakravarty, K., and P. E. Raj, 2013: Raindrop size distributions and their association with characteristics of clouds and precipitation during monsoon and post-monsoon periods over a tropical Indian station. *Atmos. Res.*, **124**, 181–189, doi: 10.1016/j.atmosres.2013.01.005.

Chandrasekar, V., W. Y. Li, and B. Zafar, 2005: Estimation of raindrop size distribution from spaceborne radar observations. *IEEE Trans. Geosci. Remote Sens.*, **43**, 1078–1086, doi: 10.1109/TGRS.2005.846130.

Chang, W. Y., T. C. C. Wang, and P. L. Lin, 2009: Characteristics of the raindrop size distribution and drop shape relation in typhoon systems in the western Pacific from the 2D video disdrometer and NCU C-band polarimetric radar. *J. Atmos. Oceanic Technol.*, **26**, 1973–1993, doi: 10.1175/2009JTECHA1236.1.

Chen, B. J., Y. Wang, and J. Ming, 2012: Microphysical characteristics of the raindrop size distribution in Typhoon Morakot (2009). *J. Trop. Meteor.,* **18**, 162–171, https://jtm.it mm.org.cn/en/article/doi/10.3969/j.issn.1006-8775.2012.02.006.

Chen, B. J., Z. Q. Hu, L. P. Liu, et al., 2017: Raindrop size distribution measurements at 4,500 m on the Tibetan Plateau during TIPEX-III. *J. Geophys. Res. Atmos.*, **122**, 11092–11106, doi: 10.1002/2017JD027233.

Gorgucci, E., G. Scarchilli, V. Chandrasekar, et al., 2000: Measurement of mean raindrop shape from polarimetric radar observations. *J. Atmos. Sci.*, **57**, 3406–3413, doi: 10.1175/1520-0469(2000)057<3406:momrsf>2.0.co;2.

Gorgucci, E., G. Scarchilli, V. Chandrasekar, et al., 2001: Rainfall estimation from polarimetric radar measurements: Composite algorithms immune to variability in raindrop shape–size relation. *J. Atmos. Oceanic Technol.*, **18**, 1773–1786, doi: 10.1175/1520-0426(2001)018<1773:Refprm>2.0.Co;2.

Gorgucci, E., V. Chandrasekar, V. N. Bringi, et al., 2002: Estimation of raindrop size distribution parameters from polarimetric radar measurements. *J. Atmos. Sci.*, **59**, 2373–2384, doi: 10.1175/1520-0469(2002)059<2373:Eorsdp>2.0.Co;2.

Houze, R. A. Jr., 2010: Clouds in tropical cyclones. *Mon. Wea. Rev.*, **138**, 293–344, doi: 10.1175/2009mwr2989.1.

Huang, J. C., C. K. Yu, J. Y. Lee, et al., 2012: Linking typhoon tracks and spatial rainfall patterns for improving flood lead time predictions over a mesoscale mountainous watershed. *Water Resour. Res.*, **48,** doi: 10.1029/2011wr011508.

Ishimaru, A., 1991: *Electromagnetic Wave Propagation, Radiation, and Scattering*. Prentice-Hall, London, 637 pp.

Ji, L., H. N. Chen, L. Li, et al., 2019: Raindrop size distributions and rain characteristics observed by a PARSIVEL disdrometer in Beijing, northern China. *Remote Sens.*, **11**, 1479, doi: 10.3390/rs11121479.

Kidd, C., A. Becker, G. J. Huffman, et al., 2017: So, how much of the earth's surface *is* covered by rain gauges. *Bull. Amer. Meteor. Soc.*, **98**, 69–78, doi: 10.1175/BAMS-D-14-00283.1.

Kruger, A., and W. F. Krajewski, 2002: Two-dimensional video disdrometer: A description. *J. Atmos. Oceanic Technol.*, **19**, 602–617, doi: 10.1175/1520-0426(2002)019<0602:TDVDAD>2.0.CO;2.

Lee, G. W., 2006: Sources of errors in rainfall measurements by polarimetric radar: Variability of drop size distributions, observational noise, and variation of relationships between *R* and polarimetric parameters. *J. Atmos. Oceanic Technol.*, **23**, 1005–1028, doi: 10.1175/JTECH1899.1.

Liu, D. F., L. Pang, and B. T. Xie, 2009: Typhoon disaster in China: Prediction, prevention, and mitigation. *Nat. Hazards*, **49**, 421–436, doi: 10.1007/s11069-008-9262-2.

Lu, X. Q., H. Yu, M. Ying, et al., 2021: Western North Pacific tropical cyclone database created by the China Meteorological Administration. *Adv. Atmos. Sci.*, **38**, 690–699, doi: 10.1007/s00376-020-0211-7.

Maki, M., T. D. Keenan, Y. Sasaki, et al., 2001: Characteristics of the raindrop size distribution in tropical continental squall lines observed in Darwin, Australia. *J. Appl. Meteor.*, **40**, 1393–1412, doi: 10.1175/1520-0450(2001)040<1393:cotrsd>2.0.co;2.

Seliga, T. A., and V. N. Bringi, 1976: Potential use of radar differential reflectivity measurements at orthogonal polarizations for measuring precipitation. *J. Appl. Meteor.*, **15**, 69–76, doi: 10.1175/1520-0450(1976)015<0069:Puordr>2.0.Co;2.

Skwira, G. D., J. L. Schroeder, and R. E. Peterson, 2005: Surface observations of landfalling hurricane rainbands. *Mon. Wea. Rev.*, **133**, 454–465, doi: 10.1175/mwr-2866.1.

Tang, Q., H. Xiao, C. W. Guo, et al., 2014: Characteristics of the raindrop size distributions and their retrieved polarimetric radar parameters in northern and southern China. *Atmos. Res.*, **135–136**, 59–75, doi: 10.1016/j.atmosres.2013.08.003.

Testud, J., S. Oury, R. A. Black, et al., 2001: The concept of "normalized" distribution to describe raindrop spectra: A tool for cloud physics and cloud remote sensing. *J. Appl. Meteor.*, **40**, 1118–1140, doi: 10.1175/1520-0450(2001)040<1118:Tcondt>2.0.Co;2.

Thurai, M., G. J. Huang, V. N. Bringi, et al., 2007: Drop shapes, model comparisons, and calculations of polarimetric radar parameters in rain. *J. Atmos. Oceanic Technol.*, **24**, 1019–1032, doi: 10.1175/jtech2051.1.

Thurai, M., V. N. Bringi, and P. T. May, 2010: CPOL radar-derived drop size distribution statistics of stratiform and convective rain for two regimes in Darwin, Australia. *J. Atmos. Oceanic Technol.*, **27**, 932–942, doi: 10.1175/2010jtecha1349.1.

Thurai, M., P. N. Gatlin, and V. N. Bringi, 2016: Separating stratiform and convective rain types based on the drop size distribution characteristics using 2D video disdrometer data. *Atmos. Res.*, **169**, 416–423, doi: 10.1016/j.atmosres.2015.04.011.

Tokay, A., and D. A. Short, 1996: Evidence from tropical raindrop spectra of the origin of rain from stratiform versus convective clouds. *J. Appl. Meteor.*, **35**, 355–371, doi: 10.1175/1520-0450(1996)035<0355:eftrso>2.0.co;2.

Tokay, A., P. G. Bashor, E. Habib, et al., 2008: Raindrop size distribution measurements in tropical cyclones. *Mon. Wea. Rev.*, **136**, 1669–1685, doi: 10.1175/2007mwr2122.1.

Ulbrich, C. W., 1983: Natural variations in the analytical form of the raindrop size distribution. *J. Appl. Meteor. Climatol.*, **22**, 1764–1775, doi: 10.1175/1520-0450(1983)022<1764:Nvitaf>2.0.Co;2.

Ulbrich, C. W., and D. Atlas, 1998: Rainfall microphysics and radar properties: Analysis methods for drop size spectra. *J. Appl. Meteor.*, **37**, 912–923, doi: 10.1175/1520-0450(1998)037<0912:rmarpa>2.0.co;2.

Ulbrich, C. W., and L. G. Lee, 2002: Rainfall characteristics associated with the remnants of tropical storm helene in upstate South Carolina. *Wea. Forecasting*, **17**, 1257–1267, doi: 10.1175/1520-0434(2002)017<1257:rcawtr>2.0.co;2.

Wang, M. J., K. Zhao, M. Xue, et al., 2016: Precipitation microphysics characteristics of a Typhoon Matmo (2014) rainband after landfall over eastern China based on polarimetric radar observations. *J. Geophys. Res. Atmos.*, **121**, 12,415–12,433, doi: 10.1002/2016jd025307.

Wang, M. J., K. Zhao, W.-C. Lee, et al., 2018: Microphysical and kinematic structure of convective-scale elements in the inner rainband of Typhoon Matmo (2014) after landfall. *J. Geophys. Res. Atmos.*, **123**, 6549–6564, doi: 10.1029/2018JD028578.

Wang, Y. Q., 2002: Vortex rossby waves in a numerically simulated tropical cyclone. Part II: The role in tropical cyclone structure and intensity changes. *J. Atmos. Sci.*, **59**, 1239–1262, doi: 10.1175/1520-0469(2002)059<1239:Vrwian>2.0.Co;2.

Wen, L., K. Zhao, G. F. Zhang, et al., 2016: Statistical characteristics of raindrop size distributions observed in East China during the Asian summer monsoon season using 2-D video disdrometer and micro rain radar data. *J. Geophys. Res. Atmos.*, **121**, 2265–2282, doi: 10.1002/2015jd024160.

Wen, L., K. Zhao, G. Chen, et al., 2018: Drop size distribution characteristics of seven typhoons in China. *J. Geophys. Res. Atmos.*, **123**, 6529–6548, doi: 10.1029/2017JD027950.

Willmott, C. J., S. M. Robeson, and K. Matsuura, 2012: A refined index of model performance. *Int. J. Climatol.*, **32**, 2088–2094, doi: 10.1002/joc.2419.

Willoughby, H. E., F. D. Marks, and R. J. Feinberg, 1984: Stationary and moving convective bands in hurricanes. *J. Atmos. Sci.*, **41**, 3189–3211, doi: 10.1175/1520-0469(1984)041<3189:Samcbi>2.0.Co;2.

Wu, D., K. Zhao, M. R. Kumjian, et al., 2018: Kinematics and microphysics of convection in the outer rainband of Typhoon Nida (2016) revealed by polarimetric radar. *Mon. Wea. Rev.*, **146**, 2147–2159, doi: 10.1175/mwr-d-17-0320.1.

Wu, Z. H., Y. Zhang, L. F. Zhang, et al., 2019: Characteristics of summer season raindrop size distribution in three typical regions of western Pacific. *J. Geophys. Res. Atmos.*, **124**, 4054–4073, doi: 10.1029/2018JD029194.

Ying, M., W. Zhang, H. Yu, et al., 2014: An overview of the China Meteorological Administration tropical cyclone database. *J. Atmos. Oceanic Technol.*, **31**, 287–301, doi: 10.1175/jtech-d-12-00119.1.

Yue, C. J., P. Y. Chen, X. T. Lei, et al., 2006: A preliminary study on method of quantitative precipitation estimation (QPE) for landfall typhoon. *Scientia Meteor. Sinica*, **26**, 17–23, doi: 10.3969/j.issn.1009-0827.2006.01.003. (in Chinese)

Zhang, G., J. Vivekanandan, and E. A. Brandes, 2001: A method for estimating rain rate and drop size distribution from polarimetric radar measurements. *IEEE Trans. Geosci. Remote Sens.*, **39**, 830–841, doi: 10.1109/36.917906.

Zhang, H. S., Y. Zhang, H. R. He, et al., 2017: Comparison of raindrop size distributions in a midlatitude continental squall line during different stages as measured by parsivel over East China. *J. Appl. Meteor. Climatol.*, **56**, 2097–2111, doi: 10.1175/JAMC-D-16-0336.1.

Zhao, K., H. Huang, M. J. Wang, et al., 2019: Recent progress in dual-polarization radar research and applications in China. *Adv. Atmos. Sci.*, **36**, 961–974, doi: 10.1007/s00376-019-9057-2.

Zheng, H. P., Y. Zhang, L. F. Zhang, et al., 2021: Precipitation microphysical processes in the inner rainband of Tropical Cyclone Kajiki (2019) over the South China Sea revealed by polarimetric radar. *Adv. Atmos. Sci.*, **38**, 65–80, doi: 10.1007/s00376-020-0179-3.

Tech & Copy Editor: Zhirong CHEN